J. Fluid Mech. (1992), *vol.* 239, *pp.* 99–132
Printed in Great Britain

Three-dimensional-mode resonance in far wakes

By T. C. CORKE, J. D. KRULL AND M. GHASSEMI
Illinois Institute of Technology, Fluid Dynamics Research Center, Mechanical and Aerospace Engineering Department, Chicago, IL 60616, USA

(Received 15 October 1990 and in revised form 22 November 1991)

This work is aimed at understanding mechanisms which govern the growth of secondary three-dimensional modes of a particular type which feed from a resonant energy exchange with the primary Kármán instability in two-dimensional wakes. Our approach was to introduce controlled time-periodic three-dimensional (oblique) wave pairs of equal but opposite sign, simultaneously with a two-dimensional wave. The waves were introduced by an array of v-component-producing elements on the top and bottom surfaces of the body. These were formed by metallized electrodes which were vapour deposited onto a piezoelectrically active polymer wrapped around the surface. The amplitudes, streamwise and spanwise wavenumbers, and initial phase difference are all individually controllable. The initial work focused on a fundamental/subharmonic interaction, and the dependence on spanwise wavenumber. The results include mode eigenfunction modulus and phase distributions in space, and stream functions for the phase-reconstructed flow field. Analysis of these shows that such a resonance mechanism exists and its features can account for characteristic changes associated with the growth of three-dimensional structures in the wake of two-dimensional bodies.

1. Introduction

The mechanisms of subharmonic instability identified by Kelly (1968) for free shear layers, by Herbert (1983*a*) for plane Poisiuelle flow, and by Craik (1971) and Herbert (1983*b*) in boundary layers are the latest additions to the family of secondary instability mechanisms in shear flows. In particular, the last three cited works are aimed at the secondary growth of three-dimensional modes, making this mechanism an important link in the chain of events governing transition to turbulence. The understanding of this process is both of fundamental interest, and a necessary step to obtaining rational approaches for controlling laminar-to-turbulent transition in these flows.

In the work described in this paper, we are interested in expanding this family of flows to include the 'far-wake' region of a two-dimensional body. By far-wake, we mean simply downstream of the point of flow reversals commonly occurring close to bluff bodies. Most past experimental work which best satisfies this requirement involved wakes of thin flat plates at zero angle of attack. One of the earliest of these was by Sato & Kuriki (1961). Using an external far-field sound source, they directly excited unstable modes in the wake. Phase measurements identified these as two-dimensional travelling waves. The spatial growth rates and mode shapes of these were reasonably predicted from a linear analysis of a base flow consisting of a Gaussian mean profile. By analysing the character of velocity time series taken at different downstream locations, they classified the evolution of the forced modes into

three regions: the linear region, the nonlinear region and the three-dimensional region. The nonlinear region was defined as beginning where the amplitudes of exponentially growing modes saturated. This region ended where the disturbances became three-dimensional. The onset of three-dimensionality was judged by a distinct change in the mode amplitude and phase distributions across the wake, and a rise in the level of spanwise velocity fluctuations.

The results of that experiment prompted Ko, Kubota & Lees (1970) to perform a finite-disturbance analysis of the stability of a two-dimensional laminar wake. This was used to explain the rapid changes observed in wake centreline velocity defect and wake half-width in the nonlinear region. In addition, it pointed out the significance of quadratic interactions which play a role in the generation of higher-harmonic modes for single-frequency conditions, and sum and difference modes for multiple-frequency inputs.

Further verification of the stability characteristics of the linear growth region came from Sato & Saito (1978) for modes induced by a far-field sound source in the wake of a slender airfoil. As with Sato & Kuriki (1961), the far-field source is expected to excite two-dimensional waves. They had also investigated the effect of multiple-frequency sources. Specifically forcing at two frequencies, above and below the natural wake instability frequency, was judged to accelerate transition. These produced discrete sum and difference modes, which further interacted with background fluctuations to yield an effective randomization. This forcing also resulted in an increase in the spreading of the wake past the nonlinear region.

Neither Sato & Kuriki (1961) or Sato & Saito (1978) observed any spanwise periodic structure in the wake. The formation of such a structure has come to be a bellwether of a three-dimensional secondary instability mechanism in the other flow fields. In transitional boundary layers, the secondary growth of oblique subharmonic wave pairs leads to a staggered array of peak and valley structures, such as has been recorded by Corke & Mangano (1989, figure 14*c*). Corresponding with this is a spanwise periodic variation in amplitude and π-shifts in the mode phase associated with the location of spanwise amplitude minima.

The first visual evidence of such features came from Cimbala (1984) and Cimbala, Nagib & Roshko (1988). They investigated the flow in the far-wake region of a circular cylinder at diameter Reynolds numbers of 140 to 150. Using both velocity sensors and flow visualization, they followed the downstream growth and decay of the initial two-dimensional vortex street, and the emergence of another structure of larger streamwise scale in the far wake. This new structure was determined to be a result of an instability of the base flow corresponding to a Gaussian mean velocity profile. This first appeared at $x/D = 100$, and was initially two-dimensional. In some cases, a three-dimensional structure with twice the streamwise wavelength then quickly emerged. Flow visualization records in the spanwise plane in one case, figure 20 of Cimbala *et al.* (1988), bear a striking resemblance to three-dimensional subharmonic secondary instability modes in boundary layers. This prompted them to question if a similar mechanism might be in play in the far wake.

A recent combined experimental and numerical investigation by Meiburg & Lasheras (1988) has looked at the development of three-dimensional vortical structures in the wake of a plane flat plate separating two equal-velocity laminar flows. In the experiment, a sinusoidal corrugation or indentation of the plate trailing edge was used to passively introduce a fixed spanwise perturbation to the two-dimensional vortex street. The three-dimensionality emerged as a three-dimensional distortion of the initially two-dimensional vortex tubes. Through the action of the

mean shear, the initial spanwise vorticity was reoriented, stretched and amplified. Qualitatively similar dynamics occurs for the initial stages of fundamental mode transition in boundary layers such as documented by Klebanoff, Tidstrom & Sargent (1962).

A recent investigation which is more relevant to the conditions for the growth of three-dimensional structures in figure 20 of Cimbala (1984) comes from Lasheras & Meiburg (1990). More specifically, we are interested in that part of their investigation that deals with three-dimensional subharmonic perturbations of the plane wake. This involved a numerical simulation of inviscid vortices for two discretized vorticity layers representing each side of the wake. The downstream evolution of the vortex sheets due to an initial perturbation consisting of a single two-dimensional wave and pairs of oblique waves, with equal but opposite spanwise wavenumbers, at the subharmonic frequency of the two-dimensional mode, resulted in patterns of three-dimensional structures which closely resembled those obtained in the flow visualization records of Cimbala. Side-view cuts through the layer in the simulation had also indicated a lack of symmetry about the wake centreline, which arose from the growth of the subharmonic wave. There was no experiment equivalent to the conditions of the inviscid model in their report.

An analytic approach was taken by Flemming (1987) in order to clarify the role of the secondary instability in the far wake. This involved the linearized secondary disturbance equations about a basic state consisting of a Gaussian mean profile and a primary two-dimensional Orr–Sommerfeld mode. This lead to a Hill-type system of equations for which several types of resonance mechanisms were expected. The results indicated that the primary instability alone cannot explain the development of three-dimensional structures in the far wake, but for sufficiently large primary disturbance amplitudes, a three-dimensional subharmonic instability can occur. The analysis also explains the lack of symmetry about the centreline of the fluctuation intensities, and presumably structure, to be a consequence of the lack of centreline symmetry of the secondary instability equations when the primary mode is symmetric.

For the Reynolds-number range of Cimbala (1984), Flemming's analysis predicts a maximum growth rate for subharmonic instability for wave pairs with wave angles of ± 66 to $\pm 68°$, with respect to the mean flow direction. At this condition, the growth rate of the three-dimensional secondary mode exceeds that of the strongest two-dimensional primary mode. In terms of the primary mode development, Flemming had also found good agreement with Sato & Kuriki (1961) as well as with the small-defect turbulent wake of Wygnanski, Champagne & Marasli (1986).

1.1. *Objectives*

The object of this work was to develop an experiment to study mechanisms for secondary growth of three-dimensional modes in the far wake of a two-dimensional body. Specifically we would focus on a parametric resonance mechanism between travelling waves consisting of a fundamental two-dimensional mode and pairs of subharmonic three-dimensional modes with equal but opposite spanwise wavenumbers. A specially designed transducer would be used to introduce the phase-locked two- and three-dimensional disturbance patterns to simultaneously seed these modes directly on the surface of the body. The methodology for introducing these would follow that used by Corke & Mangano (1989) in promoting subharmonic resonance interactions in boundary layers. We required that the disturbance input amplitudes be at levels which would guarantee an initial linear regime so as to allow

comparisons to linear theory and to the secondary instability analysis of Flemming (1986). The downstream development of each mode would be documented using two-component hot-wire measurements taken across the wake. These would be used to generate the eigenfunction modulus and phase distributions for comparison to the previous experiments and analysis. Finally, phase-averaged reconstructions of the velocity field in the plane across the wake were to be performed to give a better physical picture of the structure of the wake with controlled three-dimensional-mode growth.

2. Experimental apparatus and techniques

2.1. *Airfoil*

The wake-producing body used in this study was a NACA 0008 airfoil. It had been chosen on the criteria that it would produce a thin wake such as with a flat plate, but would be thick enough to provide room for milled slots to accommodate the oscillations of the piezoelectric film surface used to seed unstable modes. Also, since it is a simple standard shape, our experimental results obtained using it should be more readily comparable to theoretical or computational results. A schematic drawing of the airfoil and piezoelectric film covering is shown in figure 1(*a*).

The chord dimension of the airfoil was chosen to be 7.62 cm in order to maximize the active piezoelectric area to achieve sufficient forcing amplitude, as well as to provide room on the airfoil for individual conducting paths. The airfoil span was 45 cm, which was sufficient to extend outside the walls of the measurement section, where wire electrical connections were made.

The airfoil shape was cast in acrylic from a specially designed mould. This provided a body with a smooth uniform shape in span. The airfoil was also quite rigid and not susceptible to lengthwise or twisting vibration modes. In addition, it was not electrically conductive, which was a requirement for use with the piezoelectric film. Full details of the fabrication are given by Krull (1989).

The active portions of the piezoelectric film were located past the maximum thickness point, along the nearly linear portion of the airfoil shape. In this area, the surface was milled out to allow for vertical displacement of the film. The piezoelectric film was wrapped around the surface of the airfoil and stretched across the machined-out portion.

2.2. *Piezoelectric film*

The premise behind the use of the piezoelectrically active film was the creation of a device which would introduce multiple periodic disturbances directly on the surface without otherwise modifying the base flow condition. Since one of these modes was three-dimensional, a far-field sound source such as used by Sato & Kuriki (1961) or Sato & Saito (1978) was not suitable. We also wanted the ability to change the spanwise wavelength of input three-dimensional disturbances. This precluded the use of fixed passive distortions of the airfoil trailing edge, such as used by Meiburg & Lasheras (1988). In our approach, we chose a polyvinylidene fluoride (PVDF) film which is available under the name Kynar from Penwalt Corporation. The overall dimensions of the film sheet were 30 cm × 15 cm × 0.052 mm thick. Onto this film we had vapour deposited a thin layer (approximately 1000 Å thick) of a nickel–aluminium alloy in the two patterns (black) seen in figure 1(*b*), one on each side of the film. These patterns overlap so that the large common electrode only falls under the smaller rectangular electrodes, and not under the thin conducting paths.

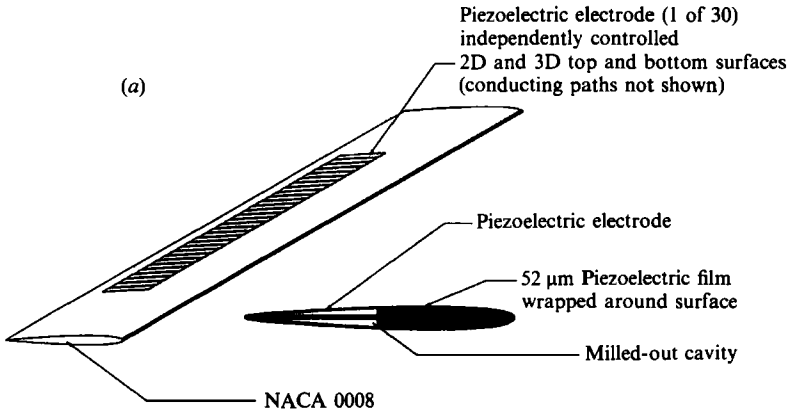

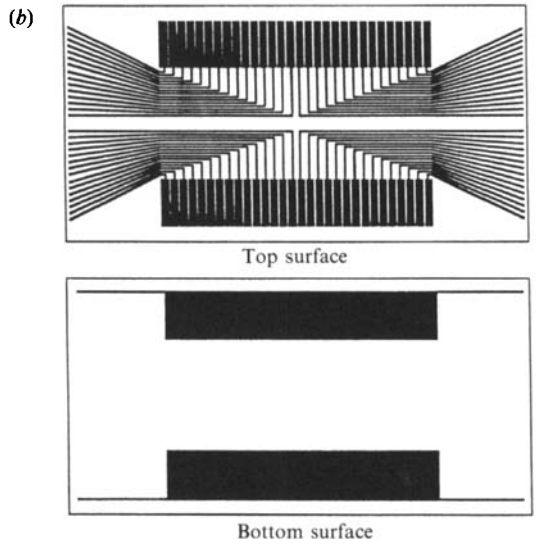

FIGURE 1. (*a*) Wake-producing airfoil with piezoelectrically active sheet wrapped around, and (*b*) schematic of metalization pattern used to excite three-dimensional modes.

Only portions of the film directly sandwiched between metal electrodes are active when a voltage is applied. These active regions (elements) elongate or contract depending on the voltage polarity. The film had been oriented so that the primary deformation direction was along the long axis of the smaller electrodes.

The elements were located over the milled-out regions on the top and bottom surfaces of the airfoil. A positive-going time series was used to excite a periodic lengthening of an element. Because of the fixed ends, this action produced a periodic outward bowing of the element. The actual direction (outward or inward) of bowing was prescribed by the polarization, in the thickness direction, of the film.

A total of 60 individually controllable elements, 30 each on the top and bottom of the airfoil, were used. The spanwise dimension of the elements was chosen so as to be able to produce oblique modes with wave angles in the range from 45° to 70°, those determined to be most amplified by Flemming (1987). The relation between the

spanwise dimension of the elements and wave angles of three-dimensional forced modes comes from Corke & Mangano (1989). This yielded a maximum dimension of 5 mm.

Each of the elements was individually controllable in amplitude, phase and frequency. The time series to the elements were provided by a digital computer which was also used for data acquisition. The method for this was the same as that used by Corke & Mangano (1989) for forcing three-dimensional-mode resonance in laminar boundary layers. Additional electronic hardware was required to amplify the voltages from the computer to the higher voltages (up to 200 V) needed to provide sufficient motion of the elements. The complete details of this are contained in the thesis by Krull (1989).

2.3. *Wind tunnel*

The airfoil was mounted through the sidewalls of the measurement section of the wind tunnel. This is a flexible, open circuit facility which is easily accessed and modified, with qualities necessary for a sensitive experiment such as this. A schematic of the measurement section is shown in figure 2 (a, b). It consists of 29.2 cm diameter cylindrical sections of transparent Plexiglas. Each section is flanged so that they can be bolted together in any desired arrangement or length. Upstream of the entrance to the measurement section are a honeycomb and series of low-solidity screens followed by a 9 : 1 area ratio contraction. The turbulence intensity at the exit of the contraction was measured to be 0.05% of the mean streamwise velocity.

In the configuration we used, the length of the measurement section was 2.3 m. The airfoil was located 0.44 m downstream of the entrance. These dimensions are shown with respect to the airfoil chord dimension in figure 2 (a, b). Velocity surveys were performed across the wakes at the centrespan location of the airfoil. The x-position range of these measurements is seen as the cross-hatched region in the figure. Flow visualization was performed using a smoke wire in the plane parallel to the airfoil span. The locations of the smoke wire and field of view are seen as the dotted region in the figure. Note that, as seen in (a), the plane of the smoke wire was displaced slightly from the wake centreplane.

A computer-controlled motorized traversing mechanism capable of moving in two directions was used to traverse the hot-wire sensor. This was located outside the measurement section, with only a probe support extending through a slot in the sidewall.

2.4. *Instrumentation and time-series processing*

A dual hot-wire sensor in an $\times$-configuration was used to measure velocity components in the streamwise (x) and cross-stream (y) directions. These were operated in a constant-temperature mode using DISA 55D01 anemometer units. The analog signals were amplified and anti-alias filtered prior to being digitized. The digital acquistion rate was 24 times the oblique mode frequency.

The data sets consisted of records of contiguous time-series points of the anemomenter outputs, at discrete y-positions across the wake for each x-position. The spatial distribution of sampled y-locations varied in order to concentrate points in the regions of largest gradients of the mean and r.m.s. fluctuation profiles. The record size and sampling rate used resulted in a total sample containing approximately 700 cycles of the fundamental mode.

Linearization of the stored anemometer voltages was performed using a third-order polynomial with best-fit coefficients determined during sensor calibration runs. The time-series velocity pairs were summed and differenced to give the respective U-

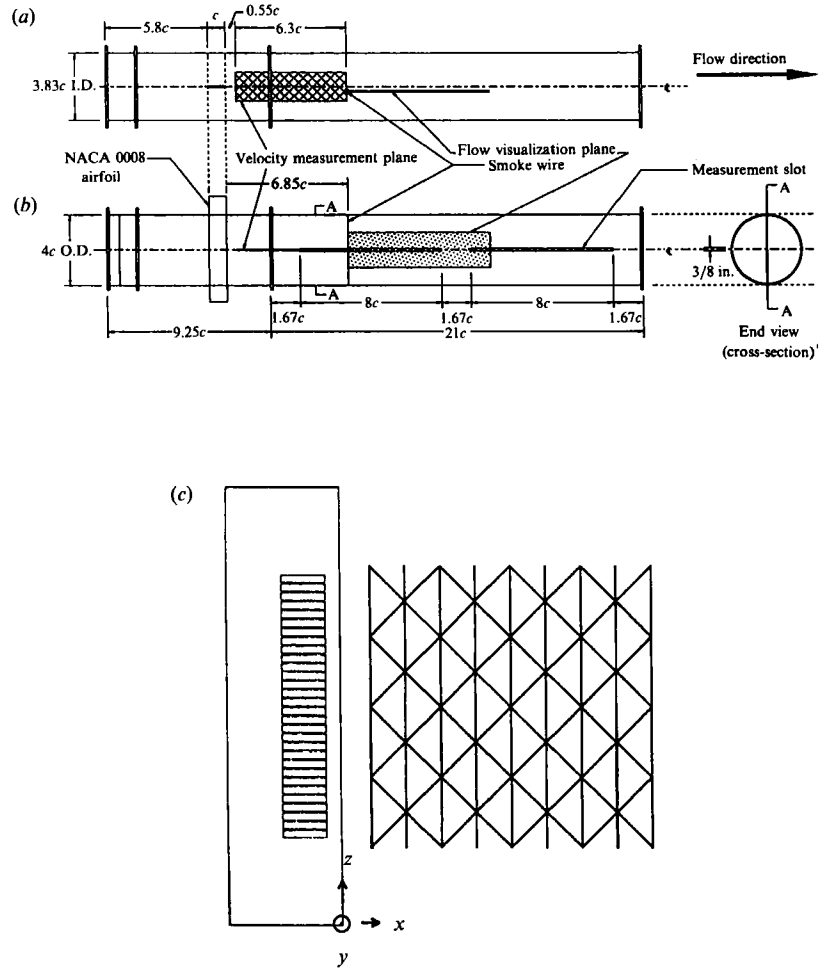

FIGURE 2. Measurement-section schematic, (*a*) top view, (*b*) front view; and (*c*) laboratory coordinate frame. $c = 7.62$ mm = 3 in.

and v-velocity component values. The eigenfunction modulus and phase distributions were determined from computations of the cross-spectra at each spatial location. The reference time series in these cases corresponded to that of the most upstream x-location on the wake centreline.

Since the data series were acquired in phase with the mode forcing, with 24 samples per subharmonic cycle, phase-averaged velocity series were easily obtained. These phase-averaged time series in the (y, x)-plane formed the basic set used for calculation of U, v-velocity stream function, z-component of vorticity, and velocity tracer particle distributions presented in the results.

3. Base flow conditions

Our purpose was to simulate Reynolds-number conditions similar to those of Cimbala (1984). In the far wake, where the mean velocity profile is Gaussian, a convenient form of the wake Reynolds number is $Re_w = \lambda U_0 b/\nu$, where b is the wake half-width and λ is a wake-deficit parameter equal to $(U_0 - U_c)/U_0$. Here U_0 is the

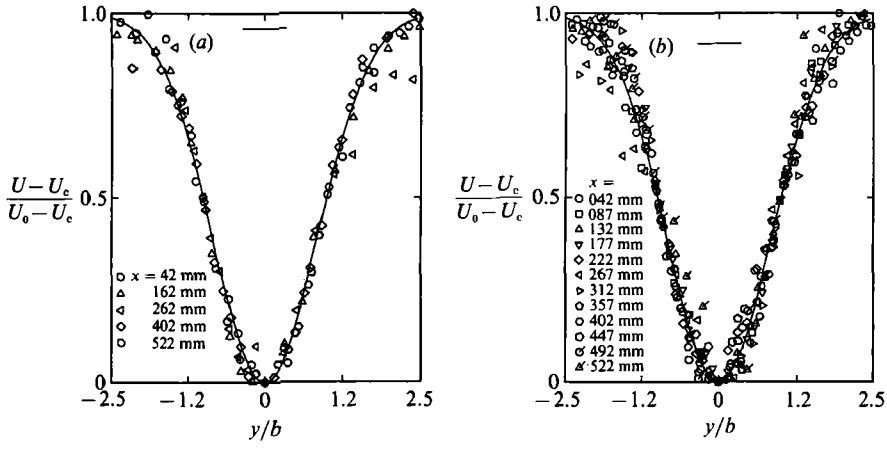

FIGURE 3. Normalized mean velocity profiles at different downstream distances in (*a*) the natural (unforced) wake and (*b*) with J-condition forcing. The curve is the Gaussian distribution, which corresponds to $\exp(-0.693y^2)$.

free-stream velocity and U_c the centreline velocity. We chose as a representative x-position, 1.5 chord lengths downstream of the airfoil ($x = 117$ cm), where $b = 2.2$ mm and $\lambda = 0.33$. The free-stream velocity was kept fixed at 2.59 m/s. This gave a wake Reynolds number value of $Re_w = 119$.

The Reynolds number, based on cylinder diameter, at which the emergence of three-dimensional modes was best documented by Cimbala (1984) was $Re_d = 150$, past $x/D = 100$. Using that position as a reference, with $U_0 = 1.52$ m/s, $b = 1.25d$, $d = 1.6$ mm and $\lambda = 0.26$, the wake Reynolds number was $Re_w = 50$. In Sato & Kuriki's (1961) work $Re_w = 450$. Therefore our value falls in the range between these two experiments. We chose to be closer to a value of 100 since most of the stability calculations of Flemming (1987) corresponded to that wake Reynolds number.

The mean profiles for the natural wake at five downstream locations which bracket the range of x-positions examined are presented in figure 3(*a*). These show good self-similarity when normalized by the local centreline velocity, U_c, and the wake half-width. The curve corresponds to the Gaussian distribution, $\exp(-Ay^2)$, with $A = 0.693$ taken from Sato & Kuriki (1961). The comparison to the Gaussian form is very good, especially for $-1.2 \leqslant y/b \leqslant 1.2$.

Another measure of the wake development is the downstream growth of the wake half-width. This is seen for the natural wake as the solid-filled symbols in figure 4. Theory predicts an increase in the half-width proportional to the square-root of the downstream distance. The theoretical curve is plotted as the dashed line. For the natural wake, the data bracket this downstream development reasonably well.

An indication of the background conditions and modes which make up the unsteady character of the wake can be obtained by viewing autospectra of velocity fluctuations across the wake. These are shown in figure 5 for the u- and v-velocity components at $x = 162$ mm. They are presented in a three-dimensional perspective view with frequency on the horizontal axis, amplitude on the vertical axis, and normalized position across the wake in the depth axis. The amplitude axis is presented as the r.m.s. level, on a linear scale, as a percentage of the free-stream speed, U_0.

The spectra show energy in velocity fluctuations only within the wake region. These fluctuations appear within three relatively broad peaks centred at ap-

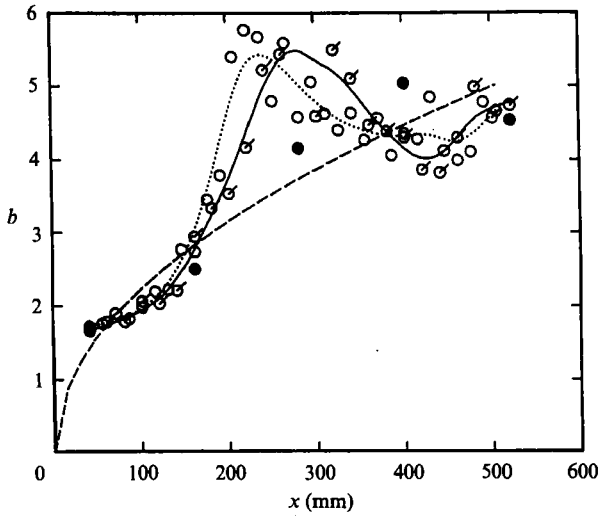

FIGURE 4. Downstream growth of wake half-width for the natural (●, ---) and two forced conditions: ○, ..., J; ⊘, ——, A.

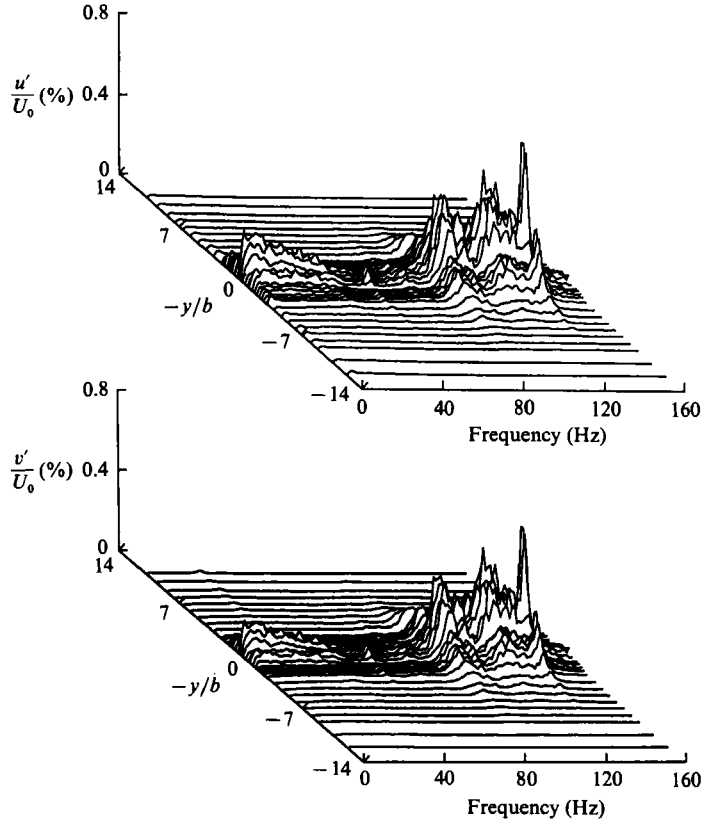

FIGURE 5. Velocity spectra components taken at different positions across the wake, at a fixed x-position of 162 mm in the natural (unforced) conditions.

proximately 104, 124 and 143 Hz. The frequency of the most amplified primary two-dimensional sinuous mode from linear temporal calculations, based on our conditions at $x = 42$ mm where $b = 1.65$ mm, is 129 Hz. This corresponds closely to the frequency of the centre peak in the spectra. Now, the peak in the theoretical growth rate curve is relatively flat so that a range of frequencies from 110 to 148 Hz have amplification rates which are within 2% of the maximum. This range encompasses well the band of frequencies observed here. We therefore believe these modes to be due to the natural instability of the wake.

What is the origin of three modes in the most amplified range, rather than the single strong mode we would expect for a two-dimensional wake? In fact, by adjusting the velocity slightly lower or higher, we could achieve a sharp single peak in the velocity spectrum in the wake. In a plot of Strouhal number versus Reynolds number, our conditions corresponded to a small region of Strouhal-number discontinuity, such as was the focus of a recent paper by Williamson (1989). The discontinuity results in frequency sidebands, such as we observe here, and a general lowering of energy in the principle mode. Williamson attributes these to cylinder end effects which result in shallow-angle oblique mode shedding.

In our case, we have deliberately positioned ourselves to be at the Reynolds number of this discontinuity in order that the natural shedding mode be weakened. This allows us to easily overwhelm the natural mode with our forced modes without having to use such large initial amplitudes that we would have little or no linear amplification region, which would have violated one of our objectives. The proof of our success should be apparent when we compare the spectra from the unforced wake to that with time-periodic forcing presented in the next section.

4. Resonance forcing

The wake was forced to produce a plane (two-dimensional) mode and oblique (three-dimensional) modes so as to promote the resonant growth of the latter. In all cases the forced modes were symmetric (sinuous). The two-dimensional mode was at 100 Hz. For the conditions at the most upstream measurement location, where the average wake half-width was 1.7 mm, this corresponded to $\alpha_r C_r = 0.411$, where α_r is the streamwise wavenumber and C_r the phase velocity. This was slightly less than the value for the most amplified two-dimensional wave at this Reynolds number (0.519), although the amplification rate is only approximately 2% less. By forcing away from the most amplified, and generally naturally occurring, mode there is no question as to the origin of modes related to the forcing.

Simultaneously with the two-dimensional mode input was a three-dimensional mode consisting of oblique wave pairs with equal but opposite spanwise wavenumbers. The three-dimensional modes were always at the exact subharmonic frequency of the two-dimensional mode, $\alpha_r C_r = 0.205$. However, we have investigated two cases with oblique wave pairs with different spanwise wavenumbers. These correspond to initial wave angles of 73° and 60°, and have been denoted as J- and A-conditions. Both these fall within the most amplified range for three-dimensional mode resonance based on analysis. A summary of the conditions is given in table 1.

As mentioned, one of our principal objectives was to have forcing levels which allowed an initial linear growth region. To document this we measured the transfer function of the forcing-level input to the output of maximum velocity fluctuations for the two-dimensional mode alone, at $x = 102$ mm. The result is presented in figure

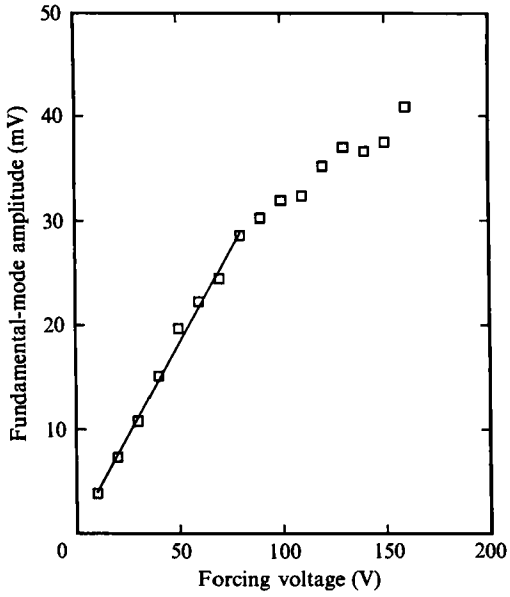

FIGURE 6. Input/output amplitude transfer function for fundamental two-dimensional mode at $x = 102$ mm.

Case	$F_{2\text{-D}}$ (Hz)	$F_{3\text{-D}}$ (Hz)	$(\alpha_r C_r)_{2\text{-D}}$ (s^{-1})	$(\alpha_r C_r)_{3\text{-D}}$ (s^{-1})	θ (deg.)	$A_{2\text{-D}}/A_{3\text{-D}}$
J	100	50	0.411	0.205	73	1.0
A	100	50	0.411	0.205	60	0.3

TABLE 1. Forcing conditions

6. In the linear regime, we expect a linear input/output relation to exist. At this x-position, this was true for forcing levels of up to 85 V peak-to-peak. We chose a 75 V forcing amplitude to ensure that a linear regime would exist, at least up to this downstream location for this mode.

From linear stability analysis (Squires theorem), we expect the oblique modes to be less amplified than the two-dimensional mode. By the same argument, the 73° wave angle mode should be less amplified than the 60° mode. We had substantiated this in the experiment where, in the linear region, the latter case experienced neutral growth, and the former decayed. The result of this was that the steeper wave required a higher initial amplitude than the other. This ensured that the three-dimensional mode was still at a sufficient amplitude, above the background fluctuations, when the two-dimensional mode had grown to its threshold amplitude for resonance to occur. This can be seen in the two-/three-dimensional-mode amplitude ratio given in table 1. For the less steep three-dimensional waves, the initial amplitude of the three-dimensional mode was one-third the size.

4.1. *Flow visualization*

A sample flow visualization record in the (x, z)-plane for a 60° wave angle (A-condition) is shown in figure 7. The plane of visualization with respect to the airfoil was shown in figure 2(a, b). The flow direction is from left to right. This photograph

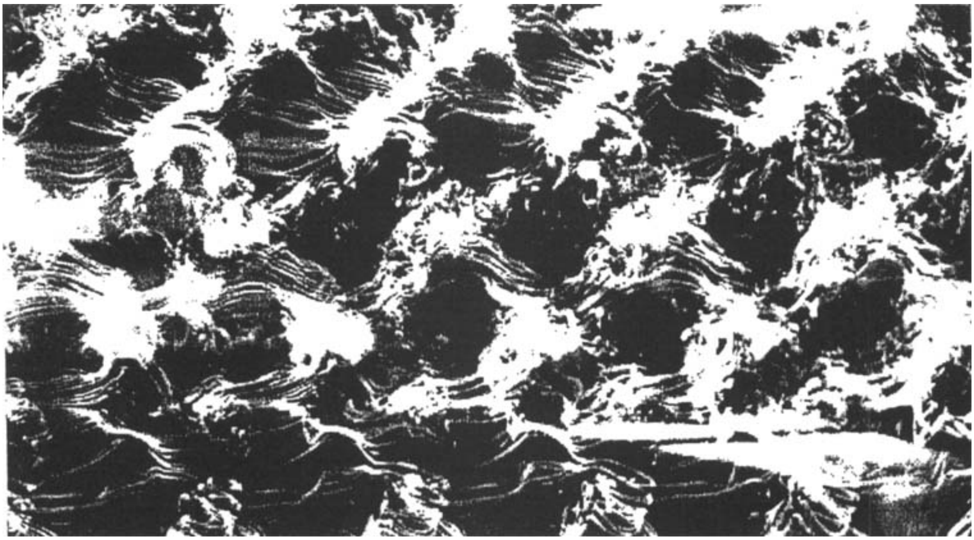

|<-------- $\lambda_{x\frac{1}{2}}$ -------->|

FIGURE 7. Sample phase-averaged smoke-wire flow visualization records for A-conditions, viewed in the (x, z)-plane. Flow is from left to right.

is actually a phase-averaged view of the approximately 25 ensembles obtained by multiple strobe-light flashes triggered in phase with the forcing time series. Photographs such as these were used to verify the spanwise structure of the flow field, and the degree of phase locking. The latter is evident by the successive overlaying of the three-dimensional pattern in space with multiple flashes of the light source. The pattern clearly shows the oblique wave pairs with crossings which are periodic in the flow (x) and spanwise (z) directions. The streamwise spacing between oblique mode crossings corresponds to the subharmonic-mode wavelength, $\lambda_{x1/2}$. The expected value based on streamwise phase measurements is shown below the photograph. The correspondence between these is good.

4.2. *Velocity surveys*

The results in this section correspond to hot-wire surveys taken across the wake. The spanwise (z) position for these measurements corresponds to the location of an oblique mode intersection. At such a spanwise position, the fluctuation amplitude of the three-dimensional mode is a maximum. For these, we will mainly focus on the J-conditions, which are generally representative of the results for the A-case.

The normalized mean velocity profiles at different x-positions, from the most upstream ($x = 42$ mm) to the most downstream ($x = 522$ mm) are shown in figure 3(*b*). Although there is some scatter, the data collapse reasonably well onto the Gaussian mean profile, represented by the solid line. The forcing conditions have therefore not altered the profile shape in a significant way, when compared to the natural (unforced) wake mean profile (figure 3*a*).

The character of the velocity fluctuations across the wake in this forced case are seen in the autospectra in figure 8. These were taken at the same x-position (162 mm) as the spectra in the natural wake in figure 5. The sharp nature of the spectral peaks, especially in the contrast to the broad peaks in the spectra for the natural wake,

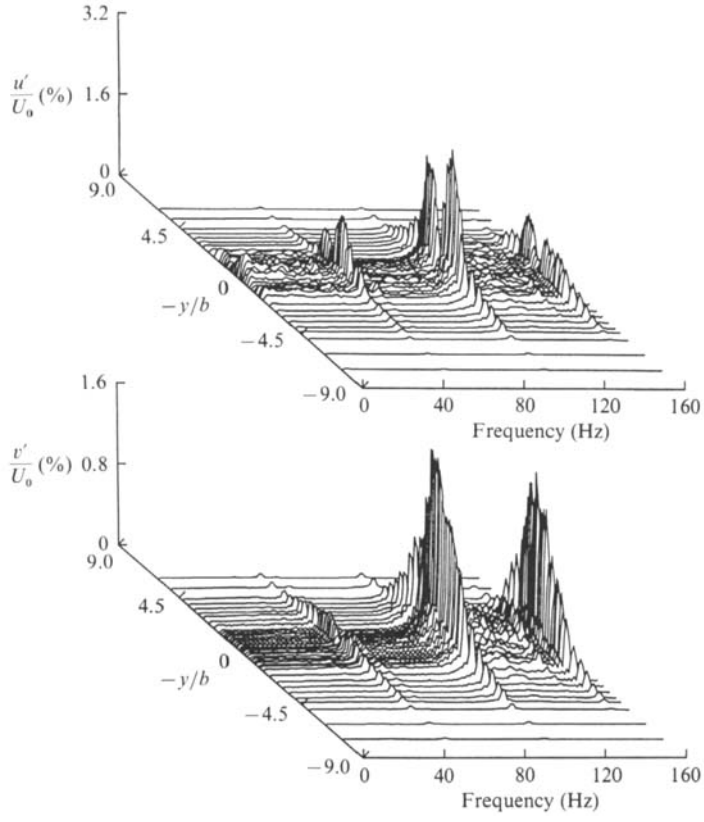

FIGURE 8. Velocity spectra components taken at different positions across the wake, at a fixed x-position of 162 mm in the forced J-conditions.

attest to the degree of control imposed by the piezoelectric transducer, and the choice of disturbance input conditions.

The spectral peaks of the two-dimensional mode, at 100 Hz, and the three-dimensional mode, at 50 Hz, are readily seen for both velocity components. The other peak at 150 Hz is a result of a summing interaction between the two input modes. The energy in these modes is clearly only concentrated in the wake of the airfoil.

One can deduce the eigenfunction modulus across the wake for each mode by drawing a curve through the spectral peaks. From these, the downstream development of the total mode energy, found by integrating the area under the eigenfunction, namely

$$U_{\text{int}} = \frac{1}{b(x)} \int_{-y\,@\,u'_0}^{+y\,@\,u'_0} u'(f, y)\,\mathrm{d}y,$$

was determined. This is shown for the u-component, for both the J- and A-conditions, in figure 9. In this figure, the open symbols correspond to the fundamental (two-dimensional) mode and the closed symbols correspond to the subharmonic (three-dimensional) mode. The data have been plotted as the log of the ratio of the amplitude in each mode as a function of downstream distance, to the amplitude of the fundamental mode at the first measurement position. For the J-conditions, the initial amplitude of the fundamental and subharmonic modes was the same, so that

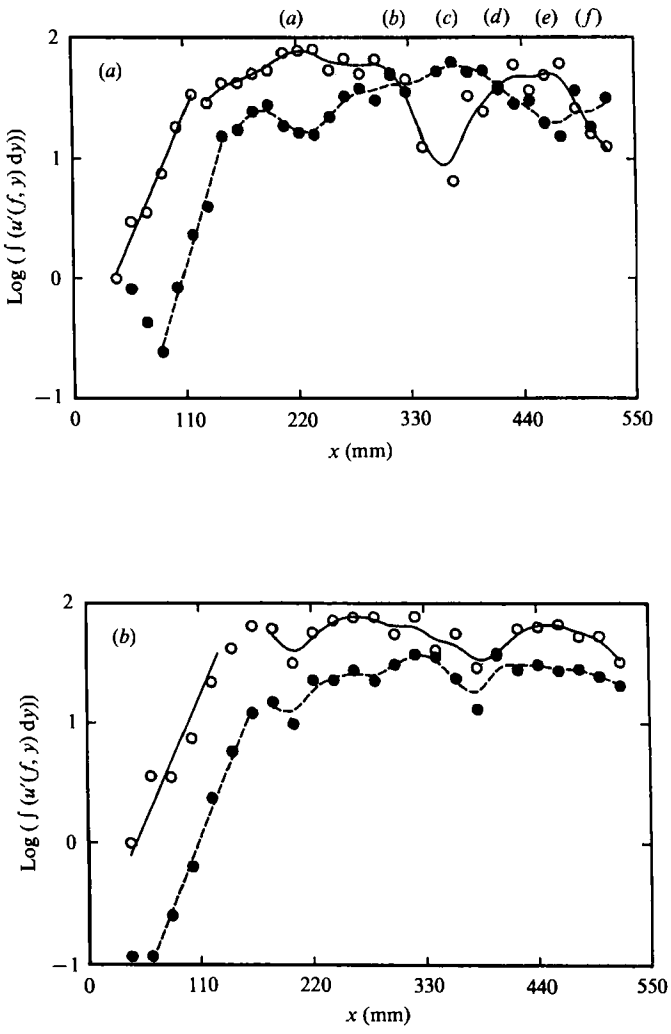

FIGURE 9. Streamwise growth of eigenfunction integrated amplitude in the fundamental and subharmonic modes for (*a*) J-conditions and (*b*) A-conditions. Open symbols correspond to the fundamental two-dimensional mode and closed symbols to the subharmonic three-dimensional mode. Positions (*a–f*) are referred to in figures 18–20.

the ratio was one (table 1). For the A-conditions, the initial amplitude of the subharmonic mode was a factor of three lower.

For the two-dimensional fundamental mode, we observe an initial region, up to $x = 110$ mm, of exponential (linear) growth. The spatial amplification rate, $-\alpha_i$, is given for that mode as the slope of the straight line (solid) in the linear regime. The line is shown with the slope $-\alpha_i = 0.206$ mm^{-1}, which corresponds to the theoretical amplification rate for a two-dimensional symmetric (sinuous) mode at this streamwise wavenumber, taken from the temporal calculation of Flemming (1987). The temporal amplification rate was given as $-\alpha_i b/U_0 = 0.137$. To extract $-\alpha_i$, we utilized the wake half-width at the first measurement location ($x = 42$ mm). The comparison to the theoretical amplification rate is observed to be excellent.

For the subharmonic three-dimensional mode, in the J-condition, the amplitude initially decays exponentially, but past the fourth x-position abruptly grows

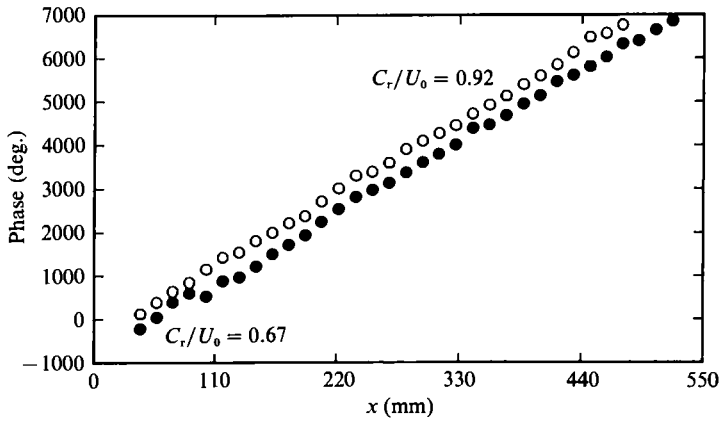

FIGURE 10. Streamwise phase development for the fundamental (○) and subharmonic (●) modes for the forced J-condition.

exponentially. The secondary growth rate of this mode is comparable to that of the two-dimensional mode. Similar behaviour occurs for the A-condition. For the less steep wave angle, the three-dimensional mode is initially neutrally growing. Past the second measurement position, this abruptly changes to a positive exponential growth, comparable to that of the two-dimensional mode.

To trace the origin of the change in amplification rate of the three-dimensional mode, we focus on their downstream phase development. The phase speed was determined from the slope of the downstream phase change relative to the reference position, at the most upstream x-location, on the wake centreline. In order to avoid the large gradients in phase occurring near the wake centreline, the downstream phase change was measured at $y/b = 5$. As a check, we also measured the downstream phase change on the other side of the wake at $y/b = -5$. This gave an identical result.

The downstream phase development for the two-dimensional fundamental and three-dimensional subharmonic modes for the J-conditions is shown in figure 10. The values for the fundamental mode (open symbols) have been plotted directly. The slope of a straight line, fit through these points is the streamwise wavenumber, α_r. The phase velocity C_r, is determined from this as $C_r = 2\pi f/\alpha_r$. If the phase velocities of these two modes are the same, the ratio of their slopes should be the ratio of their frequencies, namely 2:1. To present this better, the actual phase slope for the subharmonic mode was doubled for the presentation in figure 10 (solid symbols).

For the fundamental mode, the phase velocity is constant and equal to 92% of the free-stream speed. This value compares well to that from the calculations of Ko *et al.* (1970), which give $C_r/U_0 = 0.94$ at these relatively far downstream locations.

Initially, the phase velocity of the subharmonic three-dimensional mode is 67% (68% for the A-conditions) of the free-stream speed. Past the fourth measurement location, the three-dimensional mode adjusts its phase speed to match that of the two-dimensional mode. The phase adjustment occurs within approximately one-half of a subharmonic wavelength. The phase speed change corresponds exactly to the x-location where we first observed the secondary growth of the three-dimensional mode (figure 9*a*). This was similarly true for the A-conditions. Such a change in phase to match phase velocities, coupled with a secondary growth of an otherwise less amplified mode, satisfies the criteria for resonance. These observations are evidence that a secondary instability mechanism leading to the resonant energy exchange

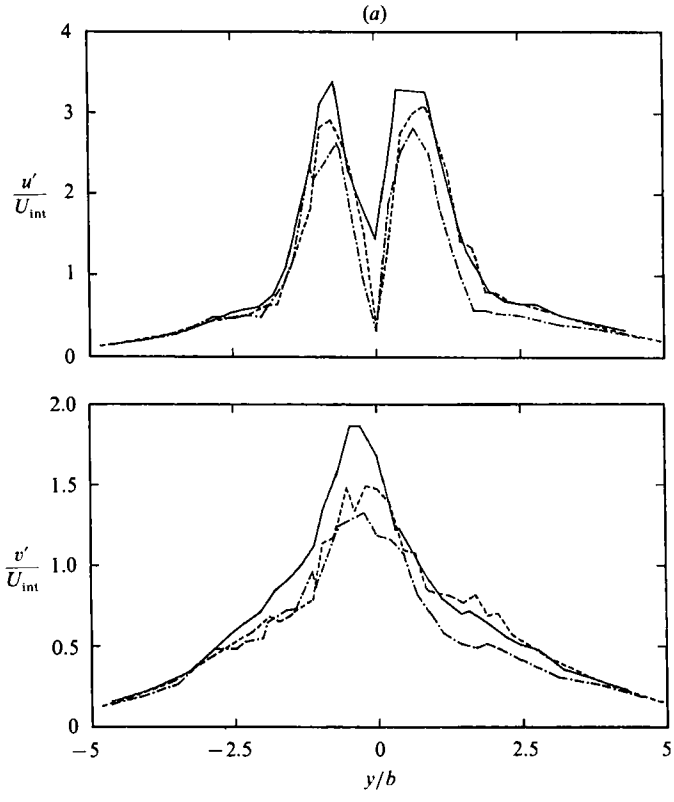

FIGURE 11(a). For caption see facing page.

between the two-dimensional fundamental and three-dimensional subharmonic modes, resulting in the enhanced growth of the three-dimensional mode, is occurring in this far wake.

The downstream evolution of the eigenfunction modulus and phase for the fundamental two-dimensional and subharmonic three-dimensional modes are presented in figures 11–15. Figures 11–13 correspond to the linear regime, upstream of energy saturation, where linear and weakly nonlinear analysis is valid. For the moduli, the downstream growth in amplitude is taken out by normalizing by U_{int}. For the phase, the curves are shifted by the local phase difference from the upstream reference, corresponding to the values plotted in figure 10.

The eigenfunctions for the two-dimensional fundamental mode in the linear regime are presented in figure 11. They show a shape which is characteristic of the symmetric two-dimensional mode, derived from linear temporal analysis such as by Sato & Kuriki (1961). In particular for the u-component, they show a double-peaked amplitude distribution with the minimum on the wake centreline, and 180° phase shift on either side of the wake centreline. For the v-component, we observe the characteristic single-peaked amplitude distribution with a maximum on the wake centreline and 0° phase shift on either side of the wake centreline. Of course, the phase shift in the v-component time series across the wake centreline defines the symmetry of initial disturbance and amplified modes.

For the fundamental two-dimensional mode, the eigenfunction modulus and phase maintain these forms, even past energy saturation. This is evident by comparing these to the further downstream distributions in figure 14(a) for the moduli, and

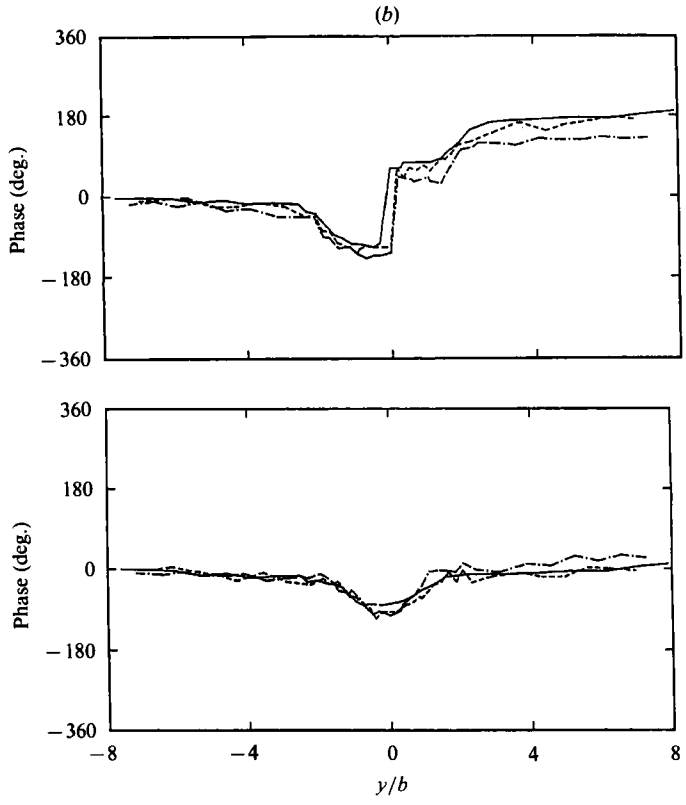

FIGURE 11. Downstream development of fundamental two-dimensional-mode eigenfunction for (*a*) amplitude and (*b*) phase for two velocity components. x-locations are within linear regime: ——, $x = 42$ mm; – – –, 57 mm; —·—·—, 72 mm.

figure 15(*a*) for the phase (u-component). The distribution from Sato & Kuriki (1961) is shown as the solid points.

The eigenfunction for the three-dimensional subharmonic mode in the linear region is shown in figures 12 and 13 for the two velocity components. We present more x-locations for this mode in order to clearly document the evolution which results from the resonant interaction with the fundamental two-dimensional mode.

By our disturbance input, the three-dimensional subharmonic mode is initially symmetric (sinuous). This is most evident from the eigenfunction phase where the v-component exhibits a 0° phase shift on either side of the wake centreline, and the u-component shows a 180° phase shift. The distribution is clear at the first three x-locations in figures 13(*b*) and 14(*b*).

In this case (J) resonance occurred at $x = 120$ mm, where the phase velocity of the subharmonic mode changed to match that of the fundamental, and enhanced growth began. In that process, the eigenfunctions evolve from ones which are characteristic of a symmetric mode to those which are characteristic of an antisymmetric (varicose) mode. Again, this is most clearly seen in the eigenfunction phase. There, in the v-component, the phase shift across the centreline is observed to gradually move from 0° to 180°. Similarly, the u-component phase shift moves from 180° to 360° (0°). This transformation from a symmetric to an antisymmetric mode shape was predicted in the analysis of Flemming (1987) as a consequence of the secondary instability process when the fundamental two-dimensional mode is symmetric.

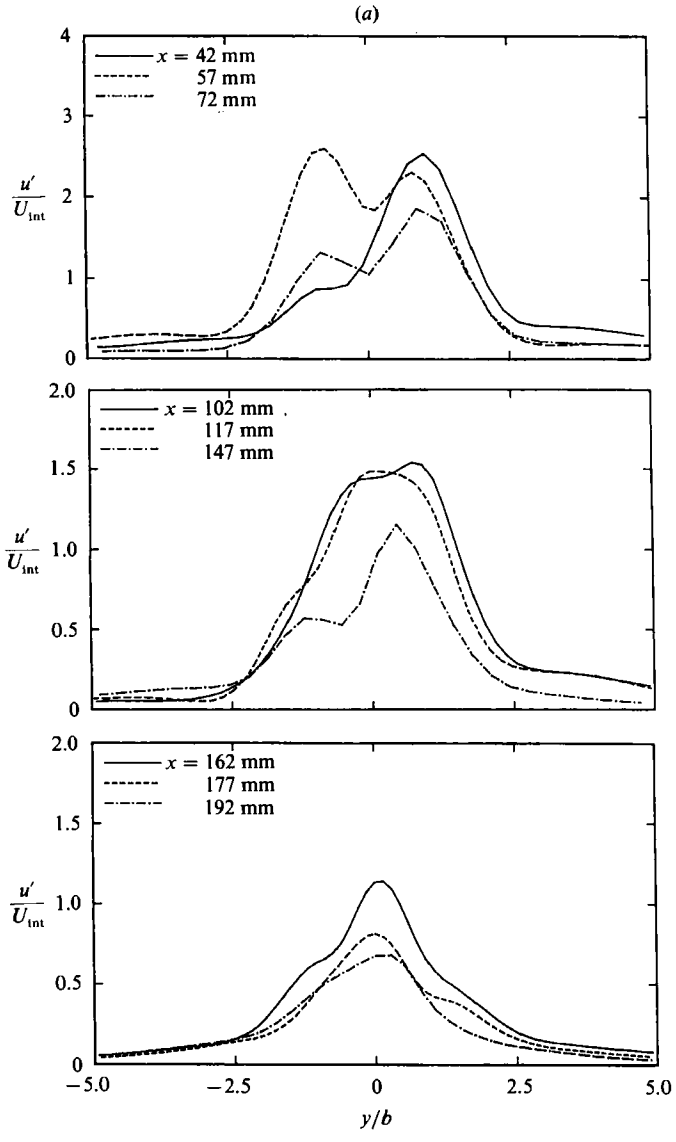

FIGURE 12(a). For caption see facing page.

In this case, beyond $x = 162$ mm to our last measurement station at $x = 507$ mm, the eigenfunction phase is self-similar. This can be seen in figure 15(*b*, *c*), which shows the phase distributions corresponding to every third x-position, starting at $x = 192$ mm. The solid points correspond to the predicted distribution from Flemming (1987). The comparison is reasonably good, especially in the v-component.

For the eigenfunction modulus, beyond $x = 162$ mm, the distribution for the v-component modulus is also reasonably self-similar. This is evident in the bottom plot of figure 13(*a*) and right plot of figure 14(*b*). In the upper right corners of each plot in figure 14(*b*) are the eigenfunction moduli from the analysis of Flemming (1985), for the respective velocity components.

Focusing on the v-component, the modulus shows two peaks, with a minimum which is displaced off the wake centreline. One of the peaks is larger in amplitude

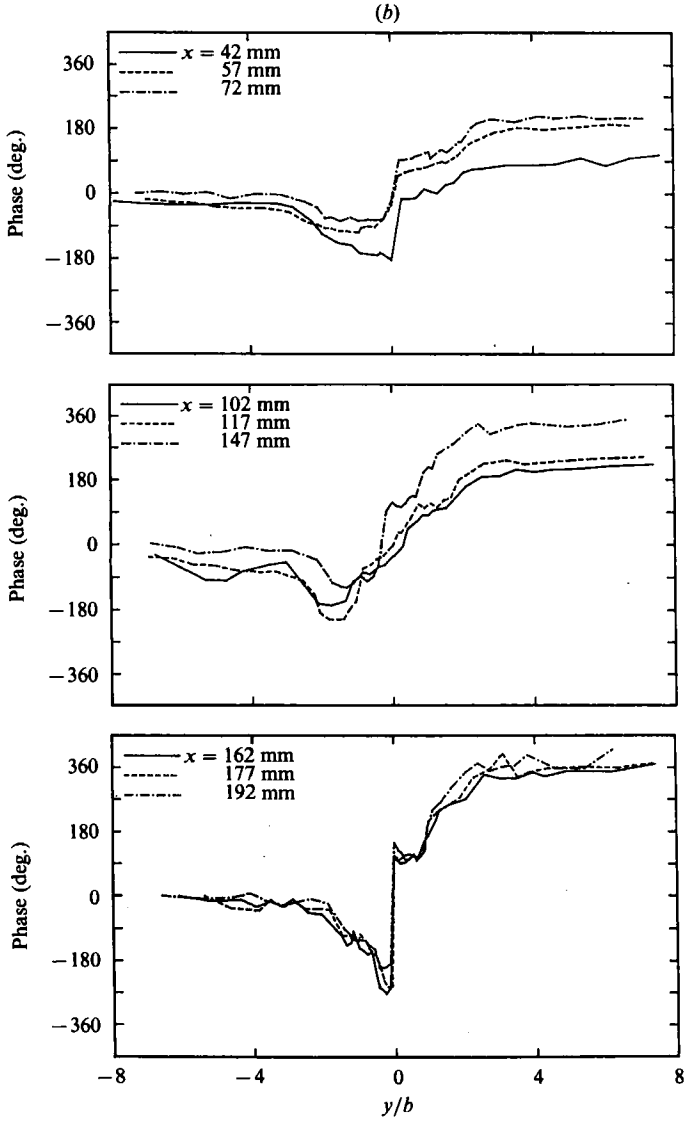

FIGURE 12. Downstream development of subharmonic three-dimensional-mode eigenfunction for (*a*) amplitude and (*b*) phase for u-component of velocity for the J-conditions; x-locations are within the linear regime.

than the other. The agreement between the shape of the measured moduli and that from the analysis is reasonably good. We note that the actual side of the wake centreline where the major peak resided appeared to shift beyond $x = 267$ mm. In figure 14, the $x = 222$ mm and 267 mm positions are rotated about the centreline to show better the degree of self-similarity.

For the u-component, the eigenfunction moduli also show two peaks with a minimum displaced from the centreline. As with the phase, the comparison to the analytic distribution for the u-component is not as good.

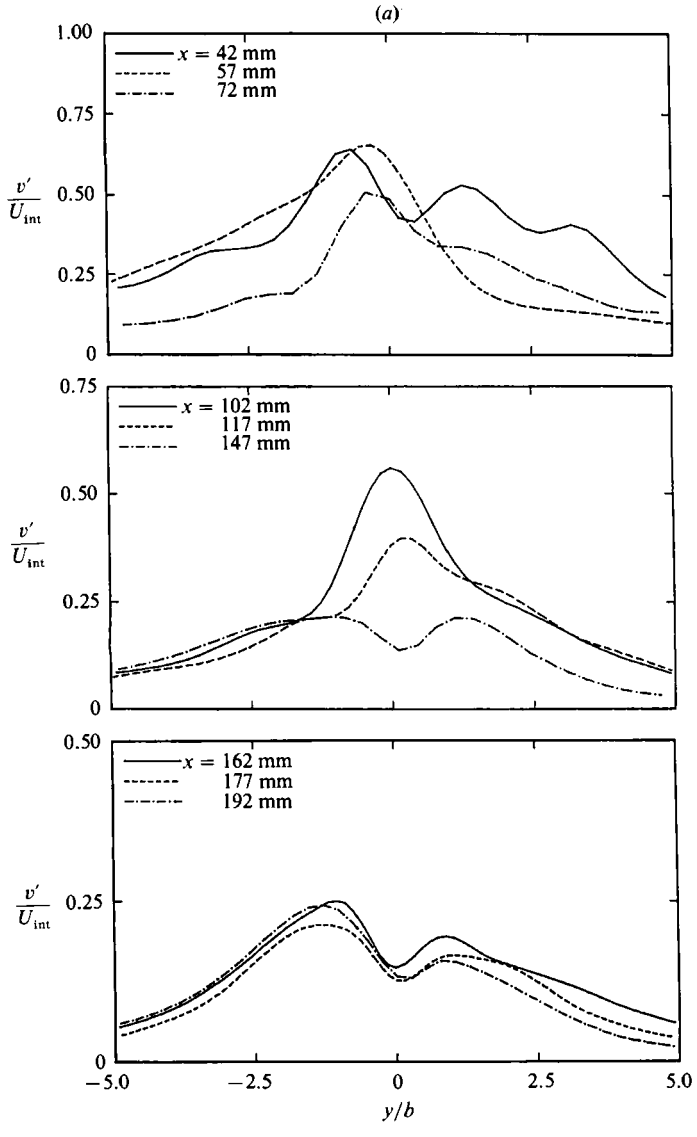

FIGURE 13(a). For caption see facing page.

4.3. *Phase-averaged picture*

In reconstructing the flow field, we were especially interested in capturing the behaviour of the wake past the point of initial energy saturation of the input modes. As the previous figures demonstrate, the eigenfunctions past the location of energy saturation maintain the same character as those in the linear and subharmonic mode secondary growth regimes. However, past energy saturation the amplitudes of these modes exhibited a cyclic growth and decay. This is best illustrated in the downstream amplitude development for the J-conditions seen in the top part of figure 9: we observe that energy in the fundamental mode first saturates at approximately $x =$ 220 mm, where its amplitude is approximately four times that of the three-dimensional mode. Past this x-location, the fundamental mode begins to decay. At the same time, the amplitude in the three-dimensional subharmonic increases, so

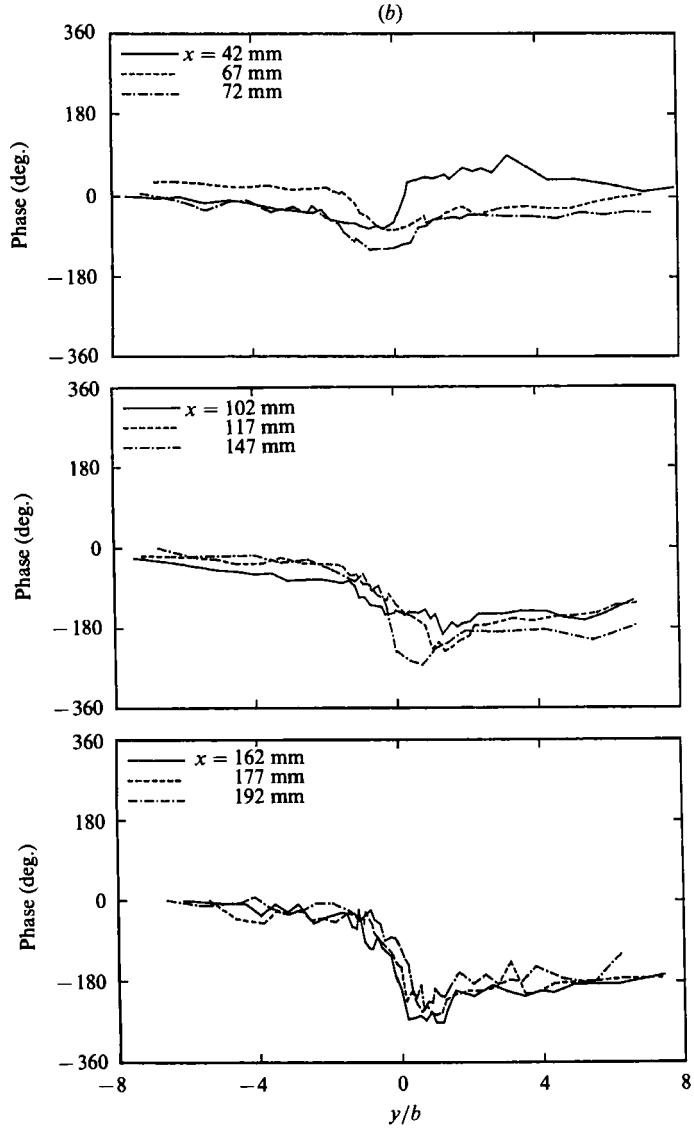

FIGURE 13. Downstream development of subharmonic three-dimensional-mode eigenfunction for (*a*) amplitude and (*b*) phase for the v-component of velocity for the J-conditions; x-locations are within the linear regime.

that $x = 350$ mm, it is the dominant mode with an amplitude approximately eight times that of the fundamental. Beyond this x-position, the amplitude of the three-dimensional mode decays, and that of the fundamental increases and again becomes dominant at $x = 440$ mm. Past this point, the cycle continues. The period of this cycle is approximately 200 mm, which corresponds to approximately 12 fundamental mode wavelengths.

Similar behaviour to this has been documented in the instability of thin shear layers of axisymmetric jets for a parametric interaction of fundamental and subharmonic axisymmetric modes. An example is seen past the linear growth region in figure 7 of Corke *et al.* (1990). In that case, less than one complete cycle can be followed. In subharmonic resonance in boundary layers, such as documented by

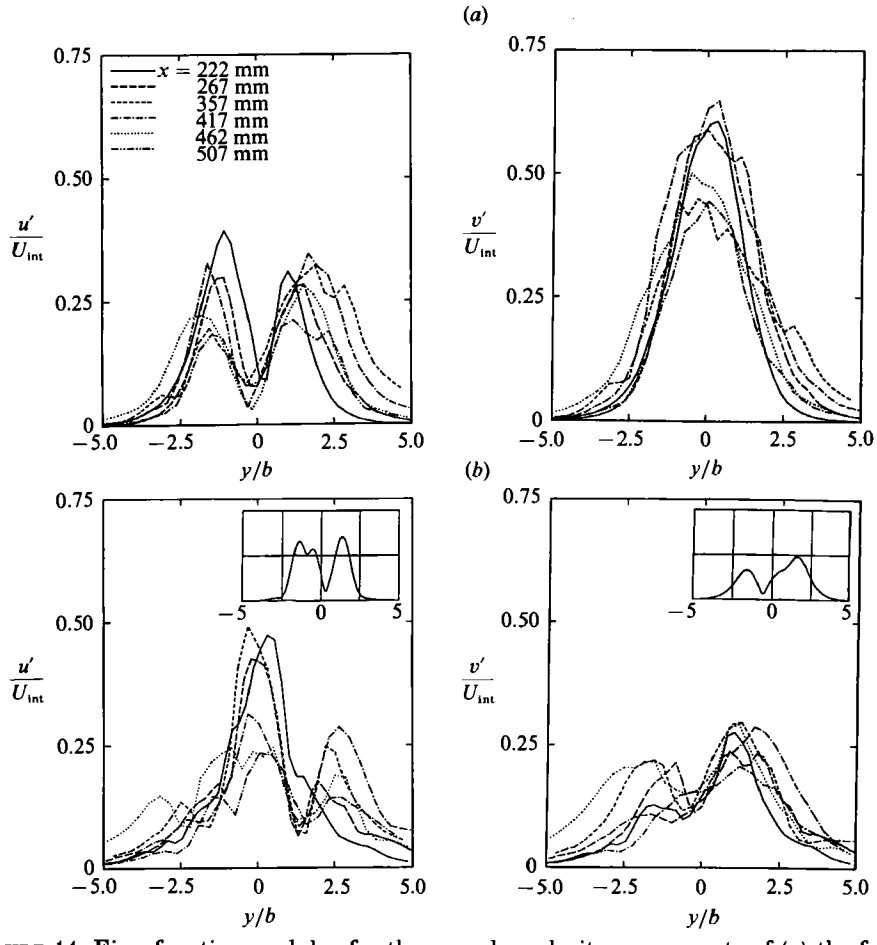

FIGURE 14. Eigenfunction modulus for the u- and v-velocity components of (a) the fundamental two-dimensional and (b) subharmonic three-dimensional modes for the J-conditions; x-locations are past the linear regime. The insets in (b) are from the analysis of Flemming (1985).

Corke & Mangano (1989), this behaviour is not generally seen. Rather, the level of the subharmonic three-dimensional mode rapidly grows to exceed that of the fundamental two-dimensional mode, and remains dominant. The slow spatial evolution of the wake then offered conditions where we could look at this stage of development, just past energy saturation, in more detail.

The method of seeding both two- and three-dimensional modes, and the use of a single computer to produce the disturbance inputs and clock the data acquisition, made it an easy task to reconstruct the unsteady flow field in a phase-averaged sense. Using the u- and v-fluctuation time series, phase-averaged vector plots, such as shown in figure 16 at $x = 267$ mm, were created. Phase averaging was done using ensemble lengths corresponding to three subharmonic cycles. This is evident in the vector plot as the three repeating structures. By comparing the features from one subharmonic cycle to the next within this figure, we also get a visual sense of the high degree of phase locking of the input modes at this x-location.

To visualize the structure of the wake in the (y, x)-plane, we followed the evolution of a sheet of tracer particles introduced at different x-locations. The sheet of particles is shown in its undeformed state in figure 17. The particles are deliberately spaced

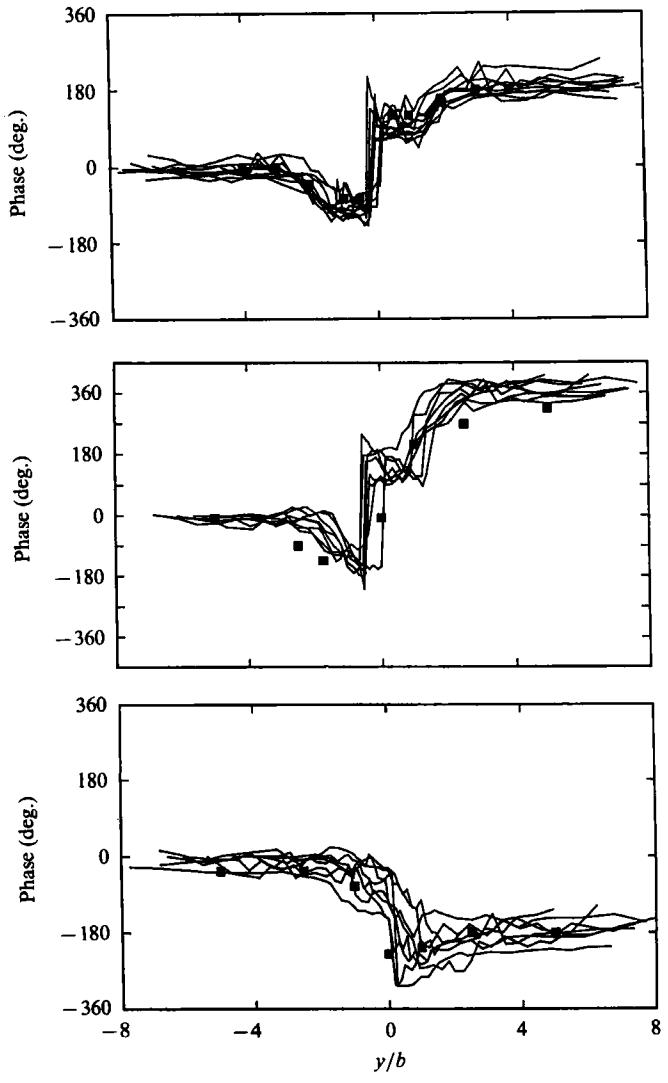

FIGURE 15. Eigenfunction phase for (*a*) the *u*-component of the fundamental two-dimensional mode, and (*b*, *c*) *u*- and *v*-components of the subharmonic three-dimensional mode for the J-conditions; *x*-locations are past the linear regime. Results of Sato & Kuriki (1961) and Flemming (1985) are shown by the solid squares in (*a*) and (*b*,*c*) respectively.

twice as closely in the centre portion of the wake in order to better show the features in the regions of the largest mean shear. The particles are transported in two-dimensional vector space, $\boldsymbol{x}$, to follow the local two-dimensional velocity vectors, $\boldsymbol{v}$, according to the relation $\mathrm{d}\boldsymbol{x}/\boldsymbol{x} = \mathrm{d}\boldsymbol{v}\,\mathrm{d}t$. The flow field includes the mean flow and phase-averaged fluctuations. The patterns that result are then due to the time-integrated paths the particles have taken from their initial position at $t = 0$.

The resulting particle distributions are shown in figure 18(*a–f*) at six x-positions, $x = 222$, 267, 357, 417, 462 and 507 mm. These positions are also denoted as (*a–f*) at the top of figure 9. They correspond respectively to the location of the first fundamental mode maximum, the first point of crossing where the fundamental mode is decaying and the subharmonic mode is growing, the location where the subharmonic mode is a maximum, the point of the second crossing, the location of

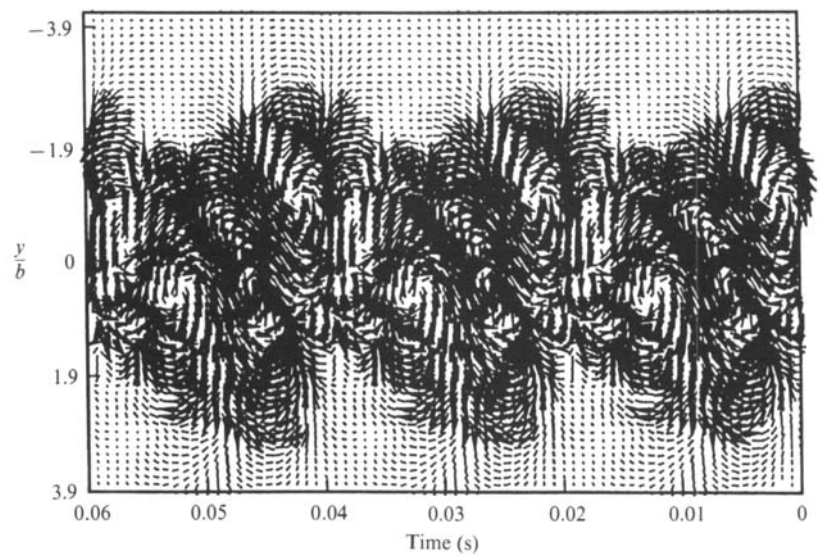

FIGURE 16. Phase-average reconstructed uv velocity vector time series across the wake at $x = 267$ mm for the forced J-condition.

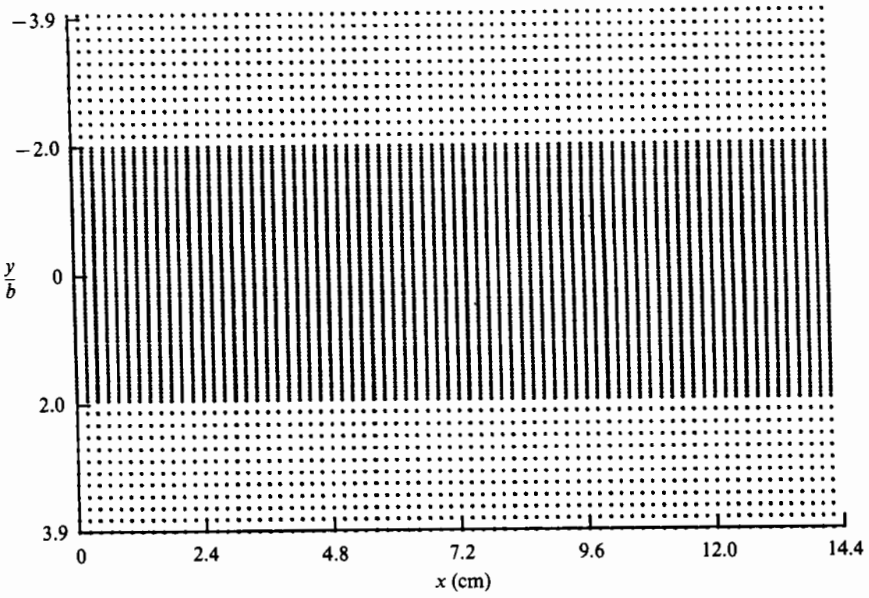

FIGURE 17. Initial positions of velocity tracer particles used in figure 18.

the second fundamental mode maximum, and the point of the third crossing. These appear in a frame of reference which is moving at the phase velocity of the fundamental and subharmonic modes, which at this point are matched (figure 10). The field of view corresponds to six fundamental (three subharmonic) mode wavelengths.

At the first x-position (222 mm), the particle patterns reveal a wave-like structure, which is principally due to the fundamental mode (six cycles). The structure due to the weaker subharmonic mode (three cycles) is also evident, especially in the line of particles at $y/b = -2$.

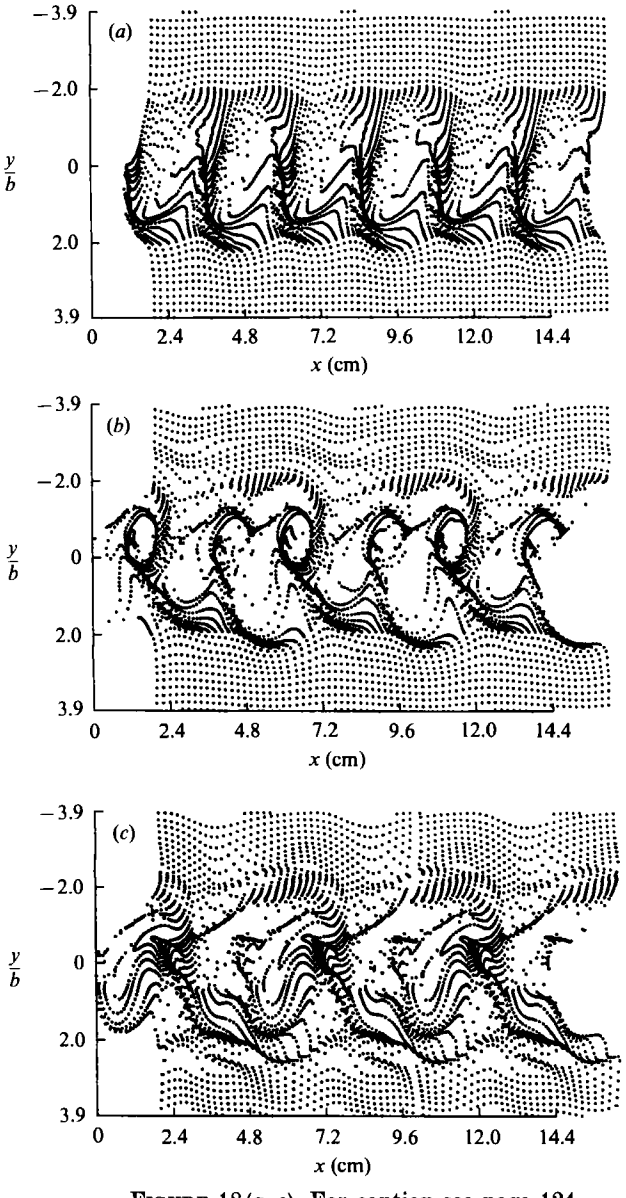

FIGURE 18(*a–c*). For caption see page 124.

At the next x-position (267 mm), the two modes are at the same amplitude. This is evident in the particle distribution in figure 18(*b*), which shows structures with a combination of the two wavelengths. A clear asymmetry in the subharmonic mode structure is also visible across the wake.

The subharmonic mode grows to a maximum at the next x-position (357 mm), figure 18(*c*). The structure of the particle distributions is now mostly due to the subharmonic mode. Since this mode is three-dimensional, this view only represents a two-dimensional cut through it. By the next x-position (417 mm), in figure 18(*d*), the amplitude of the subharmonic and fundamental modes are again the same. The particle distributions in this case look similar to the previous crossing point at $x = 267$ mm (figure 18*b*).

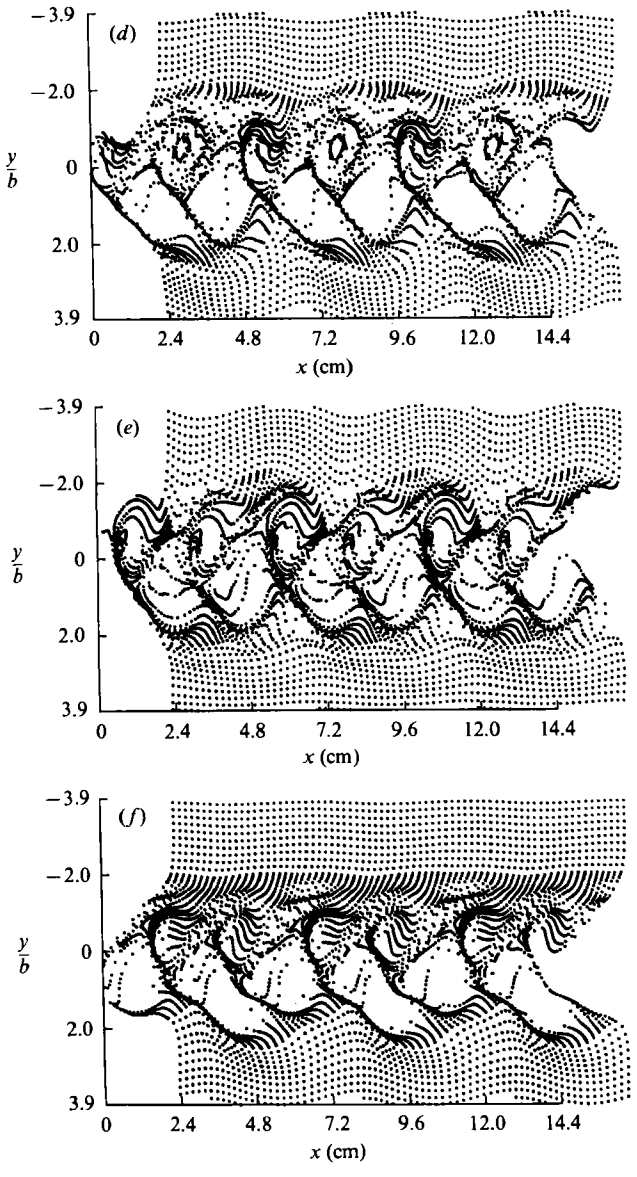

FIGURE 18. Distributions of velocity tracer particles inserted in phase-averaged velocity field at the strategic x-locations denoted in figure 9(*a*) for forced J-condition: (*a*) $x = 222$ mm; (*b*) 267 mm; (*c*) 357 mm; (*d*) 417 mm; (*e*) 462 mm; (*f*) 507 mm.

At the next x-position (462 mm), the fundamental mode is again a maximum, which is also evident in the structure of the wake in figure 18(*e*). At this stage, the fundamental mode is still believed to be two-dimensional. This is based on the fundamental-mode eigenfunction modulus and phase distributions (figures 11, 12, 14*a* and 15*a*) which maintain the features at this x-position that are characteristic of a two-dimensional mode.

The next crossing point at $x = 507$ mm (figure 18*f*) marks the return of the subharmonic mode. Again, the similarity of the structure of the wake to the previous crossing points seen in figure 18(*d*, *b*) is evident.

To see the effect of the exclusive growth and decay of these two modes on the

distribution of vorticity in the wake, we have presented in figure 19 contours of constant normalized z-component vorticity, $\omega_z b(x)/U_0$. With this normalization, the maximum absolute level of ω_z was nearly constant for all the x-locations examined. This value, corresponding to the highest contour level, was 0.1. As before, the wake is viewed in a frame of reference moving at the phase velocity of the input modes. The sense of circulation is counterclockwise for solid-line contours. The contour with absolute level closest to $\omega_z = 0$ has not been plotted for clarity.

At the most upstream location, $x = 222$ mm in figure 19(a), a wave-like vorticity distribution, with a dominant structure at the fundamental wavelength, is evident. A hint of the subharmonic mode is seen at the edges of the wake, as the slight variation of the vorticity distributions on every other structure.

At the first amplitude crossing point ($x = 267$ mm), in figure 19(b), we observe a transition to the merging of the vortical structures. The merging is complete in figure 19(c) ($x = 357$ mm), where the growth to dominance of the subharmonic mode has redistributed the vorticity to a periodic structure at its wavelength. The smaller-scale vortical structures on the outer edges of the wake appear to be associated with the $\frac{3}{2}f$ mode.

At the second transition point ($x = 417$ mm), the regrowth of the fundamental mode marks a transition to the shorter-wavelength structure. This is fully achieved by $x = 462$ mm (figure 19e). The transition to the remerging of these is seen again at the third crossing point at $x = 507$ mm (figure 19f).

4.4. *Mean flow effects*

What effect does the enhanced secondary growth of the three-dimensional mode, and periodic growth and decay past initial energy saturation, have on the mean flow in the wake? A measure of the effect on the mean flow is the downstream development of the half-width, b, which is presented for the natural and J- and A-conditions in figure 4.

As an indication of the energy transferred to or from the mean flow by the coherent motions, we calculated the distribution across the wake of the coherent mode production, $-\overline{uv}\,\mathrm{d}U/\mathrm{d}y$. This is presented in figure 20 for the same six x-locations (denoted a–f in figure 9). To show the separate contribution of each mode to the coherent mode production, the time series were first digitally bandpass filtered about each centre frequency. The distributions for the fundamental and subharmonic modes appear as the open and closed symbols, respectively.

As has been pointed out by Liu (1989), the coherent-mode production mechanism gives rise to shear-layer spreading as long as energy is transferred from the mean flow to the disturbances. This occurs when $-\overline{uv}\,\mathrm{d}U/\mathrm{d}y > 0$. At the first x-position (222 mm), just past the end of the linear growth region, a significant contribution from the mean flow goes only to the two-dimensional fundamental mode. This indicates that the secondary growth of the subharmonic mode is due primarily to an energy exchange from the fundamental mode. In addition, the growth in the wake half-width to this point is then predominantly due to the growth of the two-dimensional mode.

Past this x-location, we had observed a decrease in the wake half-width. Coincident with this was a decay in the amplitude of the two-dimensional mode and an increase in the amplitude of the three-dimensional mode. The decrease in the half-width is consistent with a decrease in the positive coherent-mode production for the fundamental mode seen in figure 20(b). This corresponds to the x-position in the vicinity of the amplitude crossing at $x = 267$ mm (position b). For the three-

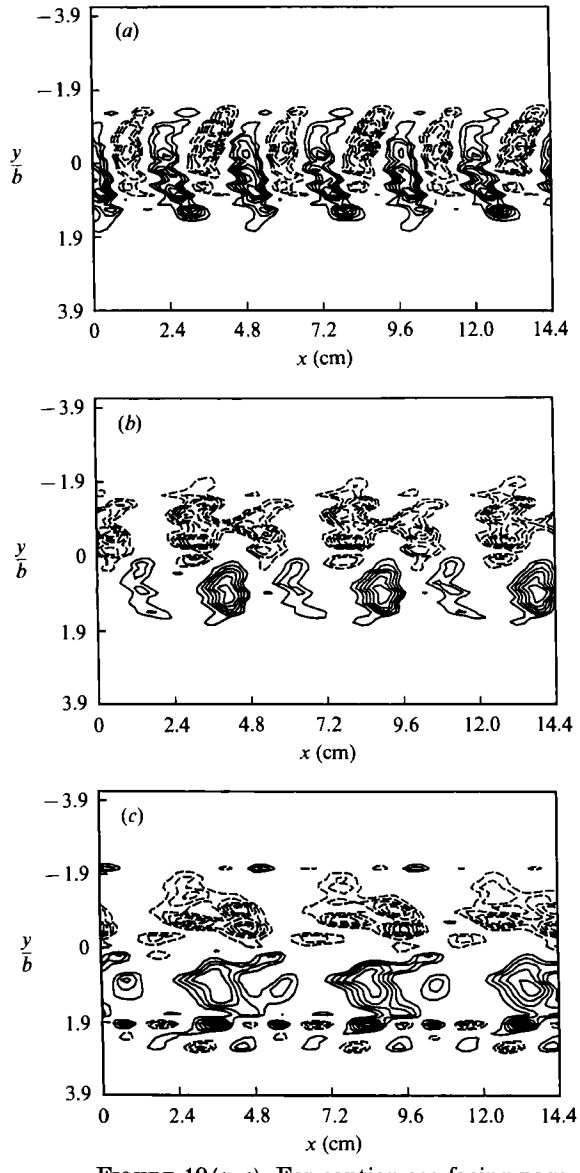

FIGURE 19(*a–c*). For caption see facing page.

dimensional mode, on the negative-y/b side of the wake centreline, a small positive value of the coherent-mode production indicates some transfer of energy from the mean flow to the subharmonic mode. This amount is relatively small so that most of the growth of the three-dimensional mode at this stage must be due to the fundamental mode. For the three-dimensional mode on the positive-y/b side of the wake centreline, the negative coherent-mode production indicates that energy is being transferred back to the mean flow. It is interesting to note that in the particle distributions at this x-position in figure 18(*b*), we observe rolled-up structures on the negative-y/b side of the wake centreline, but not on the positive side.

The asymmetry across the wake centreline in the sign of the coherent-mode production appears for both modes at the x-location of the subharmonic-mode amplitude maximum, at $x = 357$ mm, seen in figure 20(*c*). Past this x-position, the

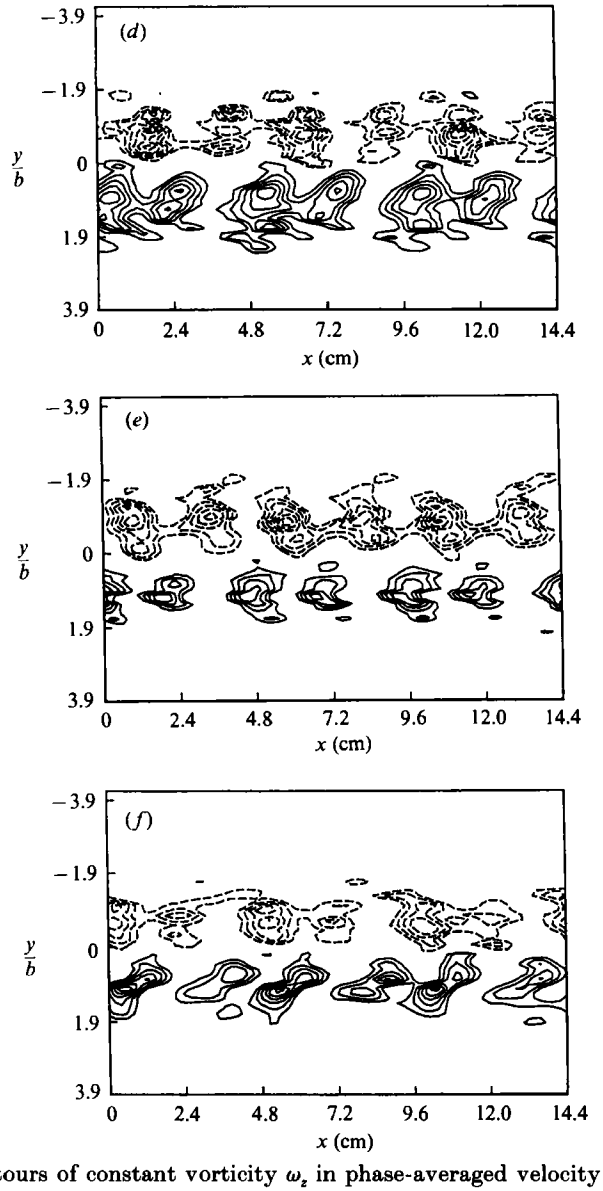

FIGURE 19. Contours of constant vorticity ω_z in phase-averaged velocity field at the strategic x-locations denoted in figure 9(*a*) for forced J-condition: (*a*) $x = 222$ mm; (*b*) 267 mm; (*c*) 357 mm; (*d*) 417 mm; (*e*) 462 mm; (*f*) 507 mm.

production term is positive for both modes, but relatively small. The regrowth of the fundamental mode at this stage is then primarily due to an energy exchange from the subharmonic.

The minimum in the total positive energy-mode production at $x = 417$ mm (figure 20*d*) corresponds to the region of the minimum wake half-width. The growth of the wake width past this point correlates well with a net positive coherent-mode production seen in figure 20(*e*, *f*). Although the distribution across the wake is not symmetric, the coherent-mode production is positive everywhere.

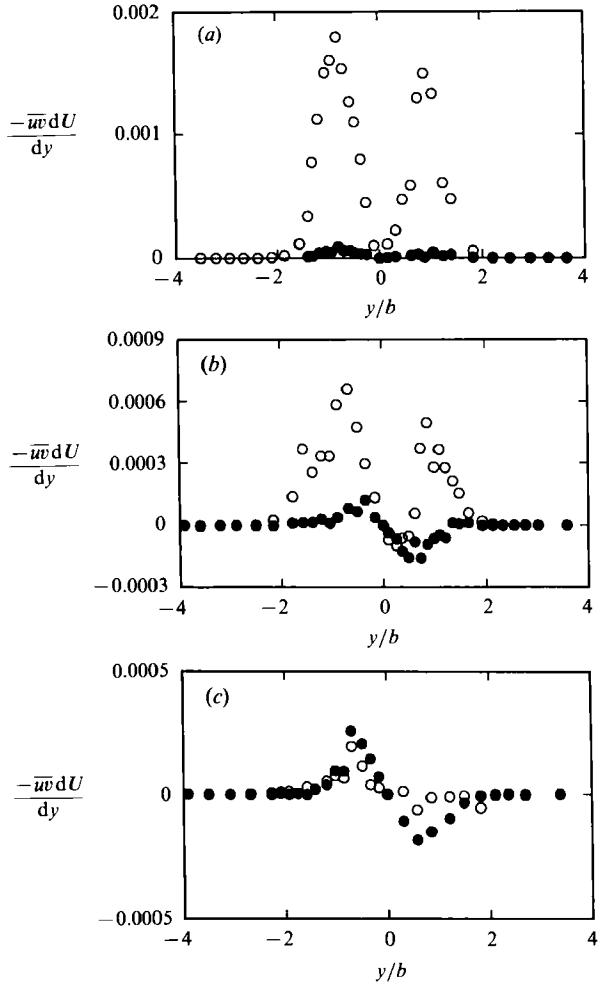

FIGURE 20(*a–c*). For caption see facing page.

5. Discussion of results

5.1. *Subharmonic resonance*

The results given in the previous section documented the enhanced secondary growth of three-dimensional subharmonic modes through a resonant (parametric) interaction with a fundamental two-dimensional mode. In an interaction of this type, the amplitude of the fundamental mode must exceed a threshold value for resonance to occur. Flemming (1987) predicted a fundamental two-dimensional-mode threshold amplitude, $A = (u'_{2\text{-D}}/U_0)/\lambda$, or approximately 15% to give a growth rate of a subharmonic three-dimensional mode comparable to that of the two-dimensional fundamental. In our case, the maximum velocity fluctuation, $u'_{2\text{-D}\max}/U_0$, at the beginning of subharmonic resonance was 1.3% and 0.3% for the J- and A-conditions, respectively. The deficit factor, λ, at this x-position was approximately 0.28, giving values for A of 4.6% and 1.1%, respectively.

In this regard, we have some discrepancy between the predicted and measured threshold levels. However, in experiments absolute levels are somewhat ambiguous since they vary with the spectral bandwidth. In our case, the levels have been

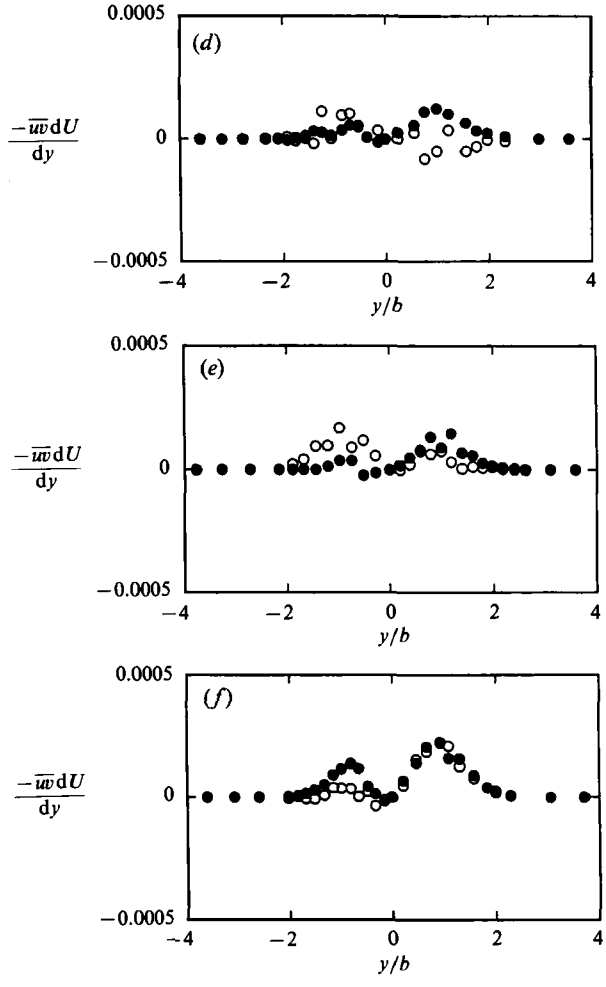

FIGURE 20. Distribution of coherent-mode production for fundamental and subharmonic modes across the wake at the strategic x-locations denoted in figure 9(*a*) for forced J-conditions: $x =$ 222 mm; (*b*) 267 mm; (*c*) 357 mm; (*d*) 417 mm; (*e*) 462 mm; (*f*) 507 mm. The fundamental and subharmonic modes are shown as open and closed symbols respectively.

converted to the standard 1 Hz bandwidth. Therefore, rather than compare absolute levels, we can look to effects of different initial conditions. These most notably are differences between the J- and A-conditions, namely their wave angles and relative amplitude, $A_{2\text{-D}}/A_{3\text{-D}}$ (table 1).

For a fixed wake Reynolds number, the secondary growth rate of a subharmonic three-dimensional mode depends both on its spanwise wavenumber (wave angle), and the amplitude of the fundamental (two-dimensional) mode. We had selected the wave angles in the two cases to approximately bracket the most amplified range. According to the analysis, at a lower fundamental mode amplitude, $A \approx 1\%$, the less steep waves (A-condition) should be more amplified. As A increases the amplification of more steep waves increases, so that at $A \approx 15\%$, those of the J-conditions should be slightly more amplified.

We find these features in the secondary growth of the subharmonic mode in figure 9. In particular, the lower threshold level required for the less steep wave condition (A) supports the fact that these are more amplified at lower fundamental amplitudes

than the steeper wave condition (J). Once resonance occurs, however, as the amplitude of the fundamental mode increases downstream, we observe a larger overall amplification rate in the more steep (J) wave condition.

A major difference between our experimental conditions and the analysis is in the choice of the streamwise wavenumber for the two-dimensional mode. In order to satisfy the slowly varying amplitude criterion for the two-dimensional mode, he selected ones which were neutrally growing. This is the customary approach (see for example Kelly 1968). In our experiment the seeded two-dimensional mode was near the most amplified. This was a consequence of the need to suppress the natural two-dimensional mode, while introducing new modes with controlled origins. Even with this difference, the comparisons to his analysis in terms of the trend in threshold amplitude, and in the eigenfunctions, especially for the v-component, are quite good.

At the point of energy saturation and beyond, the weakly nonlinear analysis is no longer valid. At this stage we had observed the two- and three-dimensional modes to undergo an exclusive, periodic growth and decay. The level of the coherent-mode energy production indicated that in this process the growth of one mode over the other was largely due to an energy exchange between them. This suggests that a simple two-equation amplitude model with couping terms, such as had been introduced by Stuart (1962), may be suitable to describe this behaviour.

5.2. *Wake structure*

The asymmetry that existed in the subharmonic eigenfunction across the wake centreline was similarly manifest in the structure of vortical motions. Given this feature of asymmetry of the vortical structures in a wake undergoing parametric three-dimensional-mode growth, we can look to flow visualization records in other experiments for evidence of this mechanism. The experiment which best shows three-dimensional subharmonic mode growth is that of Cimbala (1984), specifically his $Re_D = 150$ case in the flow visualization record reproduced in figure 20 of Cimbala *et al.* (1988). In that figure, the similarity to the patterns obtained in boundary layers undergoing three-dimensional subharmonic mode transition (for example compared to figure 14*c* of Corke & Mangano 1989) had partly motivated us to look for a similar mechanism for three-dimensional-mode growth in wakes. Unfortunately, edge-view photographs documenting the structure across the wake centreline were not available in that case. In another of their cases at $Re_D = 140$ (Cimbala *et al.*, figure 19), where edge views were available, the three-dimensional-mode structure was formed at the same streamwise wavelength as that of the upstream two-dimensional mode, not at twice the wavelength as for a three-dimensional subharmonic. In that instance, the peaks of the three-dimensional structures were also aligned in span. The aligned peak structure is a characteristic of fundamental-mode transition (K-type) in boundary layers (see for example the review by Herbert 1988). The edge-view photographs from Cimbala *et al.* in that case indicated a symmetric (sinuous) structure.

A somewhat less well-documented case in Cimbala *et al.* (1988) was for $Re_D = 190$. In this instance both spanwise and edge views of the visualized flow field existed (Cimbala *et al.*, figure 21). Although not as clearly seen, the initial formation of three-dimensional structures at the most downstream location appears to be staggered in span. The edge view shows vortical patterns which are antisymmetric (varicose) and have a tendency to roll up only on the top side of the wake. The combination of these features suggests that a three-dimensional subharmonic-mode resonance mechanism could have been operative in that case.

The inviscid vortex model of Lasheras & Meiburg (1990) with a three-dimensional subharmonic perturbation of a plane wake had also shown an asymmetry in the vortical structures across the wake centreline. In an observation similar to ours, this was seen as a preferential formation of vortices in one of the two vortical layers composing the wake. They acknowledge that this behaviour is distinctly different from that of fundamental three-dimensional-mode growth. They had not, however, observed indications of a periodic exclusive growth of the two- and three-dimensional modes, as we had in our experiment.

Finally, it is tempting to try to extend our observations of the initial three-dimensional-mode growth in laminar wakes to that in turbulent wakes. For example, Mumford (1983) found that the structures in a turbulent wake were often confined to one side of the wake centreplane rather than extending across the entire wake. Townsend (1966) had observed growth–decay cycles of large (three-dimensional) structures in turbulent wakes, which prompted his equilibrium hypothesis. The similarity to features observed here may suggest some universality in the generation of three-dimensional modes between these two flow regimes in the far-wake region of two-dimensional bodies.

6. Conclusions

The results indicate that in the far wake of a two-dimensional body, a parametric resonance between a fundamental two-dimensional mode and subharmonic three-dimensional modes can exist. Resonance was marked by an adjustment of the phase speed of the three-dimensional mode to match that of the two-dimensional mode. The point of phase-speed matching coincided with the secondary exponential growth of the three-dimensional mode. The spatial growth rate of the three-dimensional mode was nearly the same as that of the two-dimensional mode. Prior to the point of resonance, the subharmonic modes were exponentially decaying.

The eigenfunction amplitude and phase for u- and v-velocity components were found to agree well with results from past experiments and analysis. In particular, the two-dimensional fundamental-mode eigenfunction compared well with those from Sato & Kuriki (1961). The three-dimensional subharmonic-mode eigenfunction showed good agreement with those from the analysis of Flemming (1987) for a subharmonic three-dimensional mode. The eigenfunctions were distinctly different from that of the two-dimensional mode, in particular they showed an asymmetric energy and phase distribution across the wake centreline. This aspect was manifest in the shapes of vortical structures on either side of the centreplane of the wake, which was driven by the growth of the subharmonic mode.

In addition to the agreement in mode shape, the differences in threshold amplitude of the two-dimensional mode to initiate resonance in subharmonic three-dimensional modes with different spanwise wavenumbers were in agreement with analysis. The absolute threshold levels were qualitatively similar.

Beyond fundamental-mode energy saturation, the parametric resonance leads to a damped periodic exclusive downstream growth and decay of these modes. This type of behaviour may lend itself to a two-mode interaction model of the type proposed by Stuart (1962) to describe the coupled interaction of the two- and three-dimensional modes that was observed in our experiments.

This work was supported by a Grant from the Office of Naval Research, No. N00014-90-J-1420, which is monitored by Dr Edwin Rood.

REFERENCES

CIMBALA, J. M. 1984 Large structure in the far wakes of two-dimensional bluff bodies. Ph.D. thesis, California Institute of Technology.

CIMBALA, J. M., NAGIB, H. M. & ROSHKO, A. 1988 Large structure in the far wakes of two-dimensional bluff bodies. *J. Fluid Mech.* **190**, 265–298.

CORKE, T. C. & MANGANO, R. A. 1989 Resonant growth of three-dimensional modes in transitioning Blasius boundary layers. *J. Fluid Mech.* **209**, 93–150.

CORKE, T. C., SHAKIB, F. & NAGIB, H. M. 1990 Mode selection and resonant phase locking in unstable axisymmetric jets. *J. Fluid Mech.* **223**, 253–311.

CRAIK, A. D. D. 1971 Nonlinear resonant instability in boundary layers. *J. Fluid Mech.* **50**, 393–413.

FLEMMING, M. F. 1987 Secondary instability in the far wake. M.S. thesis, Illinois Institute of Technology.

HERBERT, T. 1983*a* Secondary instability in a plane channel flow. *Phys. Fluids* **26**, 871–874.

HERBERT, T. 1983*b* Subharmonic three-dimensional disturbances in unstable plane shear flows. *AIAA Rep.* 83–1759.

HERBERT, T. 1988 Secondary instabilities in boundary layers. *Ann. Rev. Fluid Mech.* **20**, 487–526.

KELLY, R. E. 1968 On the resonant interaction of neutral disturbances in inviscid shear flows. *J. Fluid Mech.* **31**, 789–799.

KLEBANOFF, P. S., TIDSTROM, K. D. & SARGENT, L. M. 1962 The three-dimensional nature of boundary-layer instability. *J. Fluid Mech.* **12**, 1–34.

KO, D. R., KUBOTA, T. & LEES, L. 1970 Finite disturbance effect on the stability of a incompressible wake behind a flat plate. *J. Fluid Mech.* **40**, 315–341.

KRULL, J. D. 1989 Three-dimensional mode resonance in far wakes. M.S. thesis, Illinois Institute of Technology.

LASHERAS, J. C. & MEIBURG, E. 1990 Three-dimensional vorticity modes in the wake of a flat plate. *Phys. Fluids* A **2**, 371–380.

LIU, J. T. C. 1989 Coherent structures in transitional and turbulent free shear flows. *Ann. Rev. Fluid Mech.* **21**, 285.

MEIBURG, E. & LASHERAS, J. C. 1988 Experimental and numerical investigation of the three-dimensional transition in plane wakes. *J. Fluid Mech.* **190**, 1–37.

MUMFORD, J. C. 1983 The structure of the large eddies in fully developed turbulent shear flows. Part 2. The plane wake. *J. Fluid Mech.* **137**, 447–456.

SATO, H. & KURIKI, K. 1961 The mechanism of transition in the wake of a thin flat plate placed parallel to uniform flow. *J. Fluid Mech.* **11**, 321–352.

SATO, H. & SAITO, H. 1978 Artificial control of the laminar–turbulent transition of a two-dimensional wake by external sound. *J. Fluid Mech.* **84**, 657–672.

STUART, J. T. 1962 Nonlinear effects on hydrodynamic stability. In *Proc. Tenth Intl Congr. Appl. Mech.* (ed. F. Rolla & W. T. Koiter), pp. 63–97.

TOWNSEND, A. A. 1966 The mechanism of entrainment in free turbulent flows. *J. Fluid Mech.* **26**, 689–715.

WILLIAMSON, C. H. K. 1989 Oblique and parallel modes of vortex shedding in the wake of a circular cylinder at low Reynolds numbers. *J. Fluid Mech.* **206**, 579–627.

WYGNANSKI, I., CHAMPAGNE, F. & MARASLI, B. 1986 On the large-scale structures in two-dimensional small-deficit turbulent wakes. *J. Fluid Mech.* **168**, 31–71.